

Design and optimization of a Tesla turbine for ORC applications

L. Talluri, D. Fiaschi*, G. Neri, L. Ciappi

Energy Engineering Dept (DIEF), University of Florence, Viale Morgagni 40/44, 50135 Florence, Italy



HIGHLIGHTS

- A novel methodology for the complete design of a Tesla turbine was developed.
- The losses were evaluated at component level.
- An innovative model for the solution of rotor flow field was applied.
- The Tesla turbine performance potential for ORC application was assessed.
- The estimation of total to static expander efficiency above 60% was achieved.

ARTICLE INFO

Keywords:

Tesla turbine
Fluid dynamics
ORC
Micro-expanders design
Pressure drop energy recovery

ABSTRACT

In recent years, small-micro power generation was appointed as one of the proper solutions to tackle the increasing energy consumption, while opening the way to distributed energy systems and micro grids. The most interesting solution for small-micro power generation is the ORC technology, however, it still needs further developments especially regarding the design of small and micro expanders. A possible solution for micro-expanders is the Tesla turbine, which is a viscous bladeless turbine. This concept was developed by Nikola Tesla at the beginning of the 20th century, but it went through a long period of indifference due to the run towards large size centralized power plants. Only recently it found a renewed appeal, as its features make it suitable for utilization in small and micro size systems, like ORC applications, where low cost components become very attractive for the exploitation of residual pressure drop.

The present study develops a design procedure of a Tesla turbine for ORC applications. A throughout optimization method was performed by evaluating the losses of each component and by introducing an innovative rotor model.

Three turbine configurations with different expander size were assessed, in order to show the performance potential of the Tesla turbine, which achieved 64% total-to-static efficiency when working with N-hexane fluid.

1. Introduction

1.1. Small power generation

The world scenario recently experienced a strong increase in energy consumption demand, associated with a series of issues related to the exhaustion, environmental impact and cost of the resources, especially for fossil fuels. This framework encourages the search of alternative energy solutions for power generation, as well as the improvement of already existing conversion systems, particularly in the field of small and medium power range, which is also the basis to move towards the direction of distributed energy systems.

The Organic Rankine Cycles (ORC) are an interesting solution in the small to medium power range, in particular when associated to low

temperature resources ($90\text{ }^{\circ}\text{C} < T < 180\text{ }^{\circ}\text{C}$). This technology utilizes organic fluids in place of steam. The Organic fluids are characterized by lower saturation temperature and pressure, and higher molecular mass when compared to steam. These properties make ORCs suitable for small-medium size power plants (50–5000 kW) and for heat recovery applications by way of gas turbine discharge [1–3], internal combustion engines [4] or industrial waste heat [5,6], as well as for energy conversion from biomass [7], solar [8] or geothermal resources [9,10] and micro-scale CHP units [11–15]. On the other hand, due to the low temperature of the resources, ORCs usually have efficiencies in the range between 8% and 20%. Therefore, the selection and the design of the expander are of paramount importance. Axial turbines are widespread used for plants with power production between 500 kW and few MWs [16], while radial turbines are better suited for the lower power

* Corresponding author.

E-mail address: daniele.fiaschi@unifi.it (D. Fiaschi).

Nomenclature		i	inlet
<i>Symbols</i>		o	outlet
\dot{m}	mass flow rate [kg/s]	PS	pressure side
a	laminar coefficient [-]	r	radial direction
A	section [m^2]	r	rotor
b	channel height [m]	Rod	Rodger
h	height of plenum chamber [m]	s	stator
h	enthalpy [kJ/kg]	t	throat
H	height [m]	t	tangential
I	rothalpy [kJ/kg]	ts	throat section
k	loss coefficient [-]	z	axial direction
L	length [m]	θ	tangential direction
Ma	Mach number	<i>Greeks</i>	
n	turbulent coefficient [-]	ζ_n	loss coefficient [-]
n_{ch}	number of rotor channels [-]	ζ_{Rod}	loss coefficient [-]
P	pressure [Pa]	ϕ_n	velocity ratio [-]
r	radius [m]	α	absolute angle [°] in radial direction
Re	Reynolds number [-]	η	efficiency [-]
s	discs thickness [m]	μ	dynamic viscosity, [kg/(m s)]
u	peripheral velocity [m/s]	ν	kinematic viscosity, [m^2/s]
v	absolute velocity [m/s]	ρ	density [kg/m^3]
w	width of plenum chamber [m]	σ	material stress [Pa]
w	relative velocity [m/s]	ω, Ω	rotational speed [rad/s]
Z	number of nozzles [-]	<i>Acronyms</i>	
<i>Subscripts</i>		CFD	Computational Fluid Dynamics
0, 1, 2, ...	reference points of expander sections	CHP	Cogeneration of Heat and Power
all	allowable	EES	Engineering Equation Solver
ch	channel	EoS	Equations of State
cl	camber line	ORC	Organic Rankine Cycle
diff	diffuser	rpm	Revolution per minute
e	enlargement	TRL	Technology Readiness Level

ranges (50–500 kW), due to their low degree of reaction and therefore their capability of dealing with large enthalpy drops at low peripheral speeds, allowing the adopting a single stage design [17–19]. Finally, for very small and micro power range applications (hW to about 50 kW), volumetric expanders, like scrolls or screws, are usually utilized, although their efficiency is limited by leakages, friction and heat transfer losses [20–22].

The comparison between various types of micro expanders for ORC applications is resumed in Table 1. As it can be noticed, in the very small power range, radial turbines are not suitable, and actually volumetric type machines are the only alternative. Among volumetric machines, scroll and rotary vane expanders are more suitable for very

small scale applications, whereas screw and reciprocating piston expanders belong to a higher power output range. Therefore, in this context, the Tesla turbine may represent a direct competitor to scroll and rotary vane expanders, as, if properly designed, it holds the same characteristics of moderate rotational speed (if relatively high rotor diameter is utilized), low manufacturing cost and suitability to very different fluids and applications. Furthermore, conversely to most of volumetric expanders, it does not require lubrication, which may be very important in several applications.

Table 1
Comparison of micro expanders for ORC applications [13,16,19–21,23]

Type	Power range [kW]	Rotational speed [rpm]	Cost	Characteristics
Scroll expander	1–10	< 10,000	Low	+ High efficiency, low cost – Lubrication requirement
Screw expander	10–200	< 10,000	Medium	+ Flat efficiency curve at off-design – Difficult to manufacture, lubrication
Reciprocating piston expander	20–100	< 12000	Medium	+ Mature technology, high pressure ratio – Heavy weight, complex
Rotary vane expander	1–5	< 10,000	Low	+ Low cost and low noise – Small power range, lubrication
Radial Inflow turbine	50–500	5,000–80,000	High	+ Light weight, mature technology – High cost, low efficiency in off-design
Tesla turbine	0.5–10	< 10,000	Low	+ Low cost, low noise, moderate efficiency, reliable – Few prototype tested (very low TRL)

1.2. Tesla turbine

Tesla turbine (also called friction or disc turbine) is a valuable candidate to play an important role in the field of small and micro power generation. This type of radial expander is characterized by the absence of rotor blades, which are replaced by multiple parallel flat disks; a little gap separates the rotor discs from the related stator parts, which consist of nozzles shaped as curved channels. The working fluid accelerates, expands through the nozzles in the stator and enters, almost tangentially, in the gaps between the disks, where it depicts a spiral centripetal path until it leaves the rotor axially at the inner radius.

Tesla turbine was patented in 1913 by the Serbian-American engineer Nikola Tesla [24]. In 1952 accurate studies for the application of this technology were performed by Armstrong [25] with the main aim of identifying the critical issues of the machine. A wider study was carried out by Rice in 1965 [26] with the realization of one of the first analytical numerical models of the flow dynamics inside the Tesla turbine. Moreover, he designed and tested six different disc turbines operating with air, discovering that the best efficiencies are achieved with small size turbines operating at low flow rates, in contrast with conventional bladed turbines. Hence Rice suggested the application of Tesla turbine to small power range, exploiting its low cost, ease of manufacture, reliability and low noise emissions. In 1991, Rice [23] summarized analytical models and experimental the results achieved in the last years, and concluded that stator efficiency is the main issue for achieving interesting levels of overall expander efficiency.

Only very recently Tesla turbine raised a renewed interest in the scientific community as expander, mainly due to the advent of micro power generation.

Several research studies were carried out to determine the analytical model of the flow inside the Tesla turbine. Carey [27,28] realized an one-dimensional idealized model of the momentum transfer in the rotor, and used it to predict the turbine efficiency in a 4 kW solar combined heat and power system based on Rankine cycle, using water as working fluid. Guha and Sengupta [29,30] developed another analytical model based on the reduction of the Navier-Stokes equations. They assumed a steady, incompressible and laminar flow, by introducing the viscosity of the fluid and a velocity gradient near the walls; this mathematical theory represents a simple but effective method for predicting the performance and efficiency of a Tesla turbine.

In recent years, also several experimental studies were conducted, mainly using steam or air as working fluids: Guha and Smiley [31] tested an improved the design of inlet and nozzles configuration by utilizing a plenum chamber and demonstrated a considerable enhancement in the uniformity of the jet, a loss in total pressure lower than 1% and an improved overall efficiency of the Tesla turbine. Hoya and Guha [32] designed and manufactured a flexible test rig for Tesla turbines. They carried out several experimental analyses, comparing various measurement methods and developed a new, simple and cheap approach (angular acceleration method) for measuring torque and power output, which overcomes the difficulties associated with the determination of very low torque at very high rotational speed. Neckel and Godinho [33] realized and tested ten convergent-divergent nozzles to improve the injection efficiency of the working fluid; the experimental test campaign was carried out with air as working fluid. Lemma et al. [34] performed a comprehensive experimental and numerical study on a 50 mm rotor Tesla turbine. The assessed efficiency of the turbine was over 20% claiming that the main causes of losses were mainly parasitic losses, in particular due to bearings. Schosser et al. [35] performed a throughout investigation of the flow field inside a Tesla turbine through a stereoscopic 3D-PTV measurement technique on a Tesla turbine working with air. The main result was the assessment of the laminar velocity profile inside the channels, which was found to slightly differ from parabolic distribution.

Other relevant experimental studies were conducted in the last

years on Tesla turbines. Bloudíček [36] dealt with the conceptual design, the 3D modelling with CAD software, the production of prototypes and the experimental assessment of machine performance. Peshlakay [37] compared different nozzles using air, water and steam, achieving 95% rotor efficiency ($\pm 9.5\%$ uncertainty) and 31% overall turbine efficiency. Krishnan [38] realized micro-turbines with diameter rotor of 1 cm using commercially available technologies and tested them with different nozzle and rotor configurations, achieving almost 40% shaft mechanical efficiency.

Tesla turbine was also analysed with computational fluid dynamics (CFD). Sengupta and Guha [39] investigated the three-dimensional flow field and the flow path lines within a Tesla disc turbine, comparing the results obtained from the analytical theory and the CFD. In a further study [40], they realized CFD analyses in order to develop similitude and scaling laws for Tesla turbines.

Schosser and Pfitzner [41] performed a throughout CFD analysis, focusing on the flow velocity profile inside an air Tesla turbine. They stated that laminar CFD results were better approximated by a fourth order polynomial function, compared to a parabolic profile.

Pandey et al. [42] carried out a computational analysis of a 1 kW Tesla turbine for pico hydropower applications. Choon et al. [43] performed an optimization analysis on a Tesla turbine with water as working fluid to exploit the energy hold within the household water supply.

Finally, Tesla turbine was considered as a suitable expander for Organic Rankine Cycle. Lampart et al. [44,45] developed a throughout CFD investigation on different size Tesla turbines with Solkatherm (SES36) as working fluid. The estimated efficiency of the turbine ranged from 30% to 50% depending on size and rotational velocity. Cirincione [46] designed and realized an ORC waste heat recovery system with a Tesla-hybrid turbine, which was claimed of being able to reach an isentropic efficiency level above 70% in steam applications; the last not reported tests were carried out with R245fa. Bao [47] defined and validated a numerical model using CFD tools to describe the flow boundary layer; then he applied it to different organic working fluids to obtain the related performance curves and concluded that the best performance can be achieved with thin gap width, in turbulent flow conditions and using fluids with high kinematic viscosity. Song et al. [48] defined a one-dimensional Tesla turbine model to predict the efficiency of a small scale ORC power plant adopting various working fluids and operating conditions: at design point, the ORC with R245ca released 1.25 kW power output at 4% thermodynamic efficiency. In 2018, Song et al. [49] improved their original one-dimensional model and compared the predicted performance to the experimental results obtained by Rice [26] with air as working fluid.

Tesla turbines have several advantages in comparison to conventional expanders for low power generation, as their relatively simple structure allows a straight manufacturing process, as well as low cost, reliability, modularity, and versatility. The machine is capable of working with both Newtonian and non-Newtonian fluids, mixed fluids, particle-laden and two-phase flows [26,23]. Moreover, the centrifugal force field ensures a self-cleaning nature and allows the usage in dirty applications like biomass and geothermal power plants, where solid particles might be present [26,23]. On the other hand, Tesla turbine presents values of efficiency lower than those of conventional turbines. The most critical aspects are the design of the nozzle and of the jet velocity profile. Several papers claim that Tesla turbine may be competitive in small and micro-scale applications [26,23,27,38,46], especially if employed in ORC power plants [48,49].

The literature review showed that several analytical and numerical models were realized, and many experimental studies were carried out, but a clear and complete design and optimization of the Tesla turbine with a model including real gas equations and concentrated pressure losses seems to be missing. Therefore, the main goals of this study are (i) the improvement of the analytical models present in literature [26,27,29,50,51], using real gas assumption while introducing sudden

expansion and contraction pressure losses and (ii) the definition of a comprehensive model for thermo-fluid dynamic and mechanical design and optimization of the expander.

2. Methodology

The Tesla turbine described and analysed in this work consists of several components: an external toroidal plenum chamber, a stator with fixed nozzles, a bladeless rotor composed by parallel thin discs fixed to the rotating shaft and a conical diffuser at the output (Fig. 1).

2.1. The plenum chamber

The plenum chamber is generally a sufficiently wide high-pressure volume. Its purpose is to decelerate the flow coming from the inlet duct, down to near-stagnation state. According to the mass balance, this is possible through a large increase in the flow cross-sectional area.

The plenum chambers are typical components in many engineering systems, but they are only modestly discussed in literature, as reported in [31,52]. Although some numerical and experimental investigations about the pressure loss and a description of the flow structure inside the volume were done [53,54], analytical models necessary to correctly design a plenum chamber and its effects on Tesla turbine performance were seldom discussed.

Smiley and Guha [31] proposed an approach for the design of the plenum chamber of the Tesla turbine based on continuity and pipe flow losses equations. In the light of the analyses of [31], it seems that the correct design of a plenum chamber for the Tesla turbine is of paramount importance. Differently from the design presented in [31], where the volume has a cylindrical shape, the plenum chamber is here developed including the turbine, with a toroidal shape, bounded by the outer case and the stator.

In order to ensure a near-stagnation state for the fluid, its velocity should be as low as possible, so that the cross section area should be fairly wide. By applying the continuity equation, the rectangular

sectional area may be calculated:

$$\dot{m} = \rho \cdot v \cdot A = \rho \cdot v \cdot (w \cdot h) \quad (1)$$

where the width w is tightly connected to the rotor parameters, and the height h , on the other hand, does not present any design constraints. A proper design of the plenum chamber ensures a reduction of total pressure losses and a uniform flow at the stator inlet.

2.2. Stator flow model

The Tesla turbine stator is made of a series of nozzles, as its purpose is the generation of the necessary tangential flow stream at rotor inlet and conversion of the pressure energy of the flow contained in the plenum to kinetic energy at nozzles output. The reduction of cross sectional area for a subsonic flow produces a favourable pressure gradient and an acceleration of the fluid [55], avoiding wall separation; as a result, the efficiency of the nozzles is usually very high, often exceeding 96% [56,57]. Anyway, for small size nozzles, in which the throat width is lower than 3 mm, the boundary layer might occupy a significant portion of the cross sectional area [58], generating increased viscous losses. In these cases, the flow is laminar ($Re < 10^5$) and the total pressure losses decrease with Reynolds number increase [58]. The stator Reynolds number is calculated at throat section with as $Re = \frac{(v_1 * H_s)}{v}$.

As discussed in several papers [25,26,31–33], the stator is commonly acknowledged to be one of the critical components of the Tesla turbine. It is one of the main causes of the machine low efficiency as assessed in several experimental tests, since it is source of high total pressure losses.

In the present study, the stator design follows the approach derived from radial expanders with vaned stators [17–19,59,60], also accounting for partial admission due to the reduced flow rates. In [18], the design guidelines for a radial ORC turboexpander are defined using a zero-dimensional model.

In order to carry out a parametric analysis, a set of geometric and

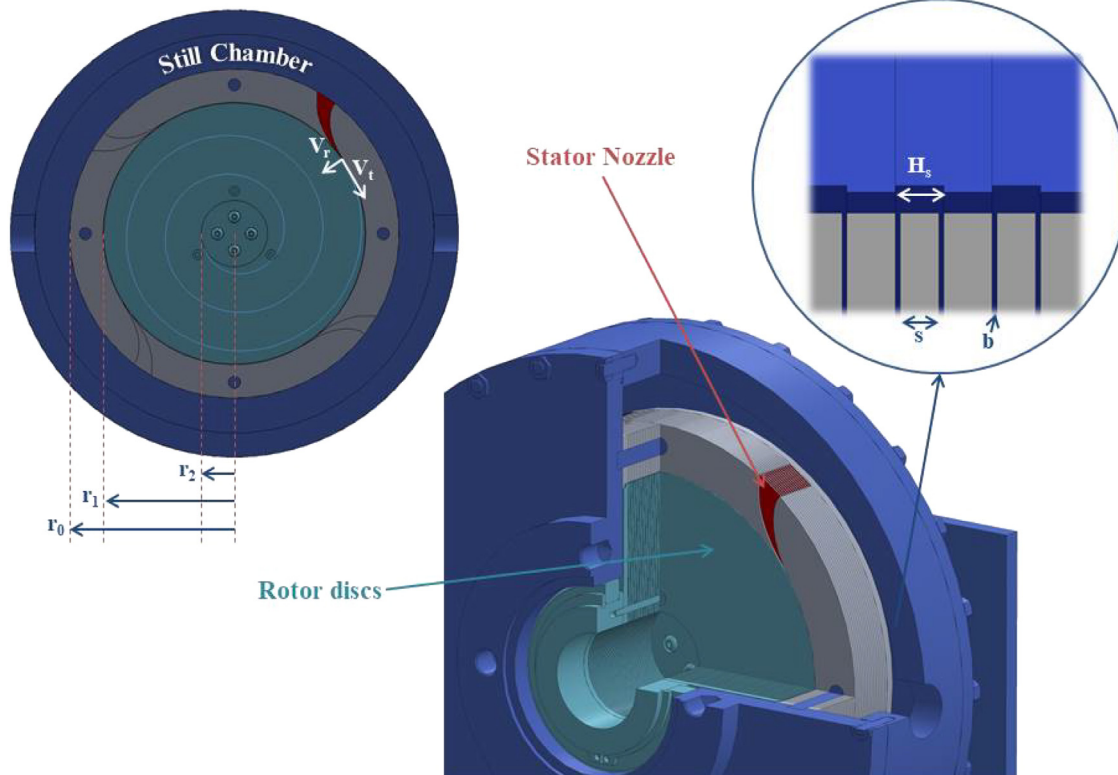


Fig. 1. Schematic of the Tesla turbine analysed.

thermodynamic parameters, need to be defined. The former are stator blade angles, number of nozzles, length and height of the channel and nozzle geometry profile, which allow the definition of the full geometry. The latter are inlet total pressure and temperature. Finally, the mass flow rate is determined once the static pressure or the Mach number at nozzle output (throat section) are provided.

The thermo-fluid dynamic model for the calculation of the fluid behaviour into the Tesla expander assumes real fluid Equations of State (EoS). For this reason, all the thermodynamic properties were evaluated as functions of couples of local variables (typically, p and T) using the Engineering Equation Solver (EES) EoS library data [61].

An iterative process on two loss coefficients was implemented. The loss factor (Eq. (2)), depending only on the velocity ratio Φ_n as reported in [62], is equalled to the loss factor presented in [63], which is a function of the stator geometry and the Reynolds number (Eq. (3)).

$$\zeta_N = \frac{h_1 - h_{1s}}{\frac{1}{2}V_1^2} = \frac{1}{\phi_n^2} - 1 \quad (2)$$

$$\zeta_{Rod} = \left(\frac{0.05}{Re} \right)^{0.2} \cdot \left(3 \cdot \frac{\tan(\alpha_l)}{(\text{pitch/chord})} + \text{pitch} \cdot \frac{\cos(\alpha_l)}{H_s} \right) \quad (3)$$

The complete scheme of the stator loss calculation model can be found in [51].

2.3. Rotor flow model

2.3.1. Basic rotor model

Inside the rotor channels, the flow expands following spiral trajectories: the components of the velocity vary steadily in modulus and direction, as a result of the pressure gradient. Since the turbine efficiency and rated power output are functions of the above-mentioned parameters, an accurate model is required to evaluate the performance of the machine.

The first developed model for the rotor flow was derived from [26,27], applying some remarkable improvements, as reported in a previous work [50]. Specifically, real and compressible fluid behaviour was considered (rather than ideal and uncompressible). The variable density and the other thermodynamic functions were taken as fluid properties, depending on the local variables (for example pressure and temperature). As for the stator model, the fluid properties were locally evaluated using EES EoS library [61]. The assumptions of steady, laminar and two-dimensional flow were kept, as well as the viscous forces were treated as body forces acting on the flow at each position [27]. It allowed simplifying and thus numerically solving the fundamental Navier-Stokes equations, expressed in cylindrical coordinates [50]. The solution was represented by the pressure and tangential velocity gradient in the radial direction.

From the momentum equation in radial direction:

$$\left(\frac{\partial p}{\partial r} \right) = -\frac{12\mu}{b^2} \left(\frac{\dot{m}}{2\pi r b \rho} \right) + \frac{\rho}{r} \left(\frac{\dot{m}}{2\pi r b \rho} \right)^2 + \frac{\rho V_\theta^2}{r} \quad (4)$$

From momentum equation in tangential direction:

$$\frac{\partial V_\theta}{\partial r} = \frac{24\mu\pi r(V_\theta - \omega r)}{b\dot{m}} - \frac{V_\theta}{r} \quad (5)$$

The rotor model was completed with the mass balance, which allows the calculation of the radial velocity:

$$V_r = -\frac{\dot{m}}{2\pi r b \rho} \quad (6)$$

The detailed set of assumptions and numerical equations are reported in [50].

Eq. (5) was numerically solved with a dedicated home built procedure in EES software, by applying a step forward method (centered finite difference): the rotor channel was discretized in radial direction

with a predefined number of equal steps. This equation set allows the calculation of the local values of pressure and velocity, both in absolute and relative coordinates. Finally, the rothalpy conservation (Eq. (7)) was applied to calculate the local value of static enthalpy:

$$h = I_i - \frac{w^2}{2} + \frac{u^2}{2} \quad (7)$$

The model was validated [50] against the data of [27,29], for incompressible fluid (constant density): the behaviour of the relative tangential velocity resembles the calculations reported in [27].

An important upgrade of the model presented in [50] was the assumption of variable viscosity in Eqs. (4) and (5) in which it was locally evaluated as a flow property as a function of temperature and pressure, using the EES fluid library data. The results obtained with N-hexane showed a limited reduction of the viscosity values (lower than 2%), due to the modest variation in fluid temperature. However, this upgrade allowed more accurate results at negligible additional calculation time.

The rotor model was completed by the calculation of the performance indicators like power output, total to static efficiency and the non-dimensional fluid dynamic parameters, such as load and flow coefficients.

2.3.2. Upgraded rotor model

An upgraded model for the rotor flow was derived from [29]. The main difference was the assumption of viscous flow in place of the equivalent body forces along the radial and tangential directions. By adopting this new approach, the Navier-Stokes equations in cylindrical coordinates further simplified; in this case, the body forces were assumed negligible, while the viscous terms were still present. Thus, the Navier-Stokes equations were reduced to:

Continuity equation:

$$\frac{1}{r} \frac{\partial (\rho r w_r)}{\partial r} = 0 \quad (8)$$

r-Momentum equation:

$$w_r \cdot \frac{\partial w_r}{\partial r} - \Omega^2 r - 2\Omega w_\theta - \frac{w_\theta^2}{r} = -\frac{1}{\rho} \frac{dp}{dr} + \nu \frac{\partial^2 w_r}{\partial z^2} \quad (9)$$

θ -Momentum equation:

$$w_r \cdot \frac{\partial w_\theta}{\partial r} + \frac{w_r w_\theta}{r} + 2\Omega w_r = \nu \frac{\partial^2 w_\theta}{\partial z^2} \quad (10)$$

z-Momentum equation:

$$\frac{\partial p}{\partial z} = 0 \quad (11)$$

The present model introduces an axial velocity profile, so that the relative velocities in r and θ directions may be expressed as:

$$w_\theta(r, z) = \bar{w}_{\theta_2} \zeta(R) G(z) \quad (12)$$

$$w_r(r, z) = \bar{w}_{r_2} \zeta(R) H(z) \quad (13)$$

where:

$$R = \frac{r}{r_2}; \quad \zeta(R) = \frac{\bar{w}_\theta(r)}{\bar{w}_{\theta_2}}; \quad \xi(R) = \frac{\bar{w}_r(r)}{\bar{w}_{r_2}}$$

$$G(z) = \frac{w_\theta(r, z)}{\bar{w}_\theta(r)}; \quad H(z) = \frac{w_r(r, z)}{\bar{w}_r(r)}$$

$G(z)$ and $H(z)$ are the variations of tangential and radial velocities respectively, along z direction within the boundary layers.

Following the procedure outlined in [29], it was initially assumed that the velocity profile of the fully developed flow was laminar and thus parabolic. Accordingly, $G(z)$ and $H(z)$ could be expressed as:

$$G(z) = H(z) = 6 \frac{z}{b} \left(1 - \frac{z}{b} \right) \quad (14)$$

Table 2
Set parameters for comparison between ANSYS and EES models.

Fluid	Air (real)
Channel mass flow rate	0.001119 [kg/s]
Inlet pressure	160,200 [Pa]
Outlet pressure	131,234 [Pa]
Rotational velocity	18,000 [rpm]
Inlet tangential velocity	118.3 [m/s]
Inlet radial velocity	5.14 [m/s]

and

$$w_r(r, z) = \bar{w}_r \cdot 6 \frac{z}{b} \left(1 - \frac{z}{b}\right) \quad (15)$$

$$w_\theta(r, z) = \bar{w}_\theta \cdot 6 \frac{z}{b} \left(1 - \frac{z}{b}\right) \quad (16)$$

By integrating the differential form of the θ -momentum and r -momentum equations between $z = 0$ and $z = b/2$, and by applying the boundary conditions reported in [29], that assume maximum velocity value at mid channel and zero velocity at the walls, it was possible to calculate the gradient of relative tangential velocity and static pressure in radial direction.

$$\frac{\partial w_\theta}{\partial r} = -\frac{5}{3}\Omega - \left(\frac{10\nu}{w_r b^2} + \frac{1}{r}\right) \cdot w_\theta \quad (17)$$

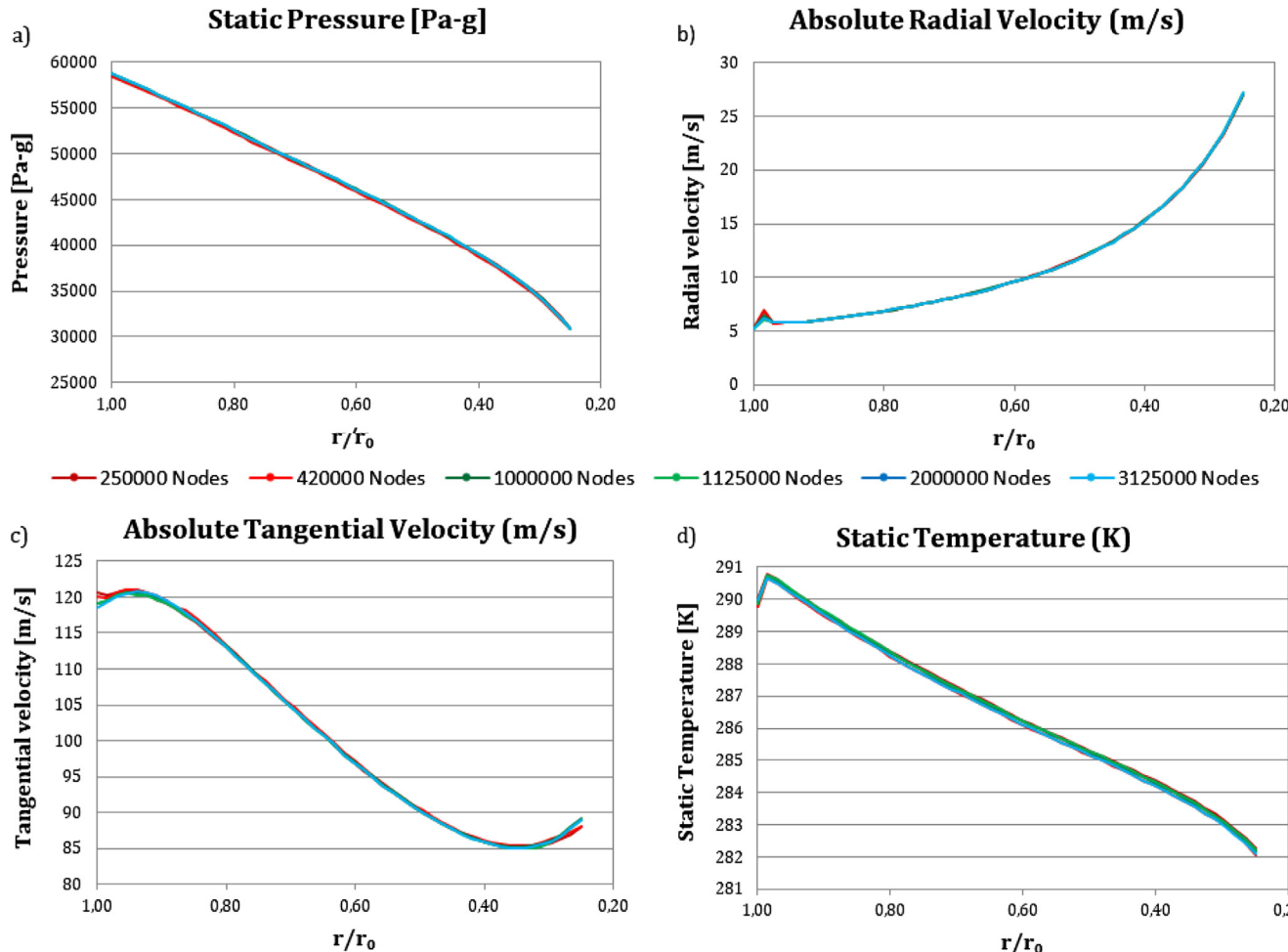


Fig. 2. Results of the mesh sensitivity analysis performed on simulations with transitional turbulence model.

$$\frac{1}{\rho} \frac{dp}{dr} = -w_r \frac{\partial w_r}{\partial r} \cdot \frac{6}{5} + \Omega^2 r + 2\Omega w_\theta + \frac{w_\theta^2}{r} \cdot \frac{6}{5} - \nu w_r \cdot \frac{12}{b^2} \quad (18)$$

In order to generalize the mathematical model of the flow, a coefficient for the parabolic velocity profile was defined, still under the assumption of laminar flow condition. Accordingly, $G(z)$ and $H(z)$ can be expressed as:

$$G(z) = H(z) = a \frac{z}{b} \left(1 - \frac{z}{b}\right) = a \frac{z}{b} - a \left(\frac{z}{b}\right)^2 \quad (19)$$

where the coefficient “a” is set equal to 6 in [29].

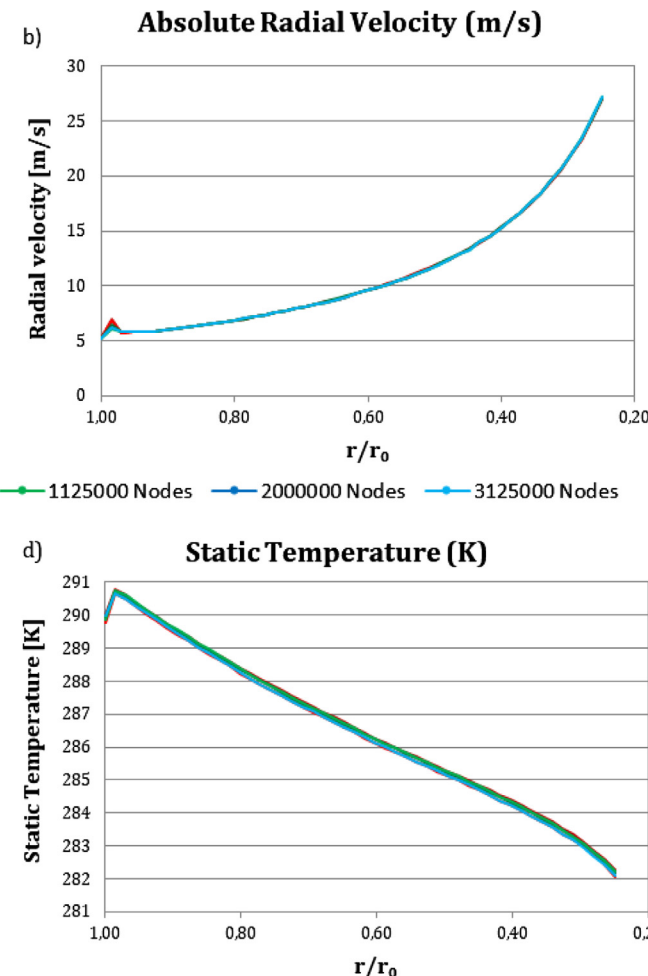
Following the above calculation steps, the reduced θ and r momentum equations were achieved and implemented into the developed EES calculation code, in the same way as for the previous case:

$$\frac{\partial w_\theta}{\partial r} = -\frac{10}{a} \Omega - \left(\frac{60\nu}{w_r ab^2} + \frac{1}{r}\right) \cdot w_\theta \quad (20)$$

$$\frac{1}{\rho} \frac{dp}{dr} = -w_r \frac{\partial w_r}{\partial r} \cdot \frac{a^2}{30} + \Omega^2 r + 2\Omega w_\theta \cdot \frac{a}{6} + \frac{w_\theta^2}{r} \cdot \frac{a^2}{30} - \nu w_r \cdot \frac{2a}{b^2} \quad (21)$$

In order to further generalize the mathematical model of the flow, a general law for the definition of the velocity profile for turbulent flows was introduced. The required constraints were the zero and the maximum velocity at the walls and at mid channel height, respectively.

The turbulent flow velocity profile law is suggested in Ref. [64]; accordingly, the applied power law distribution was adopted for the definition of $G(z)$ and $H(z)$:



$$G(z) = H(z) = \left(1 - \frac{z}{\left(\frac{b}{2}\right)}\right)^{\frac{1}{n}} \cdot \frac{(n+1) \cdot (2n+1)}{2n^2} \quad (22)$$

Following the previous calculation process, with the only difference in the integration of velocity distribution functions, it was possible to calculate the gradient of relative tangential velocity and static pressure in radial direction:

$$\frac{\partial w_\theta}{\partial r} = -2\Omega \cdot \frac{n+2}{n+1} - \left(-\frac{v}{w_r} \cdot \frac{2(2n+4)}{n^2 b^2} + \frac{1}{r}\right) w_\theta \quad (23)$$

$$\begin{aligned} \frac{dp}{dr} &= -w_r \frac{\partial w_r}{\partial r} \cdot \frac{n}{n+2} \cdot \frac{(n+1) \cdot (2n+1)}{2n^2} + \Omega^2 r + 2\Omega w_\theta \cdot \frac{n}{n+1} \\ &\quad \frac{(n+1) \cdot (2n+1)}{2n^2} + \frac{w_\theta^2}{r} \cdot \frac{n}{n+2} \cdot \frac{(n+1) \cdot (2n+1)}{2n^2} \\ &\quad + v w_r \cdot \frac{4}{nb^2} \cdot \frac{(n+1) \cdot (2n+1)}{2n^2} \end{aligned} \quad (24)$$

For fully developed turbulent flows, $n = 7$ is the most used value in literature. For this reason, the law is also called the *one-seventh power law velocity profile*.

Furthermore, for laminar flow profiles, Ref. [64] suggests the following expression for the functions $G(z)$ and $H(z)$:

$$G(z) = H(z) = 2 \cdot \left(1 - \left(\frac{z}{\frac{b}{2}}\right)^2\right) \quad (25)$$

After the required passages of integration and derivation, Eq. (25) corresponds to the generalized parabolic formula when the coefficient "a" is equal to 8.

The power law exponent, as reported in [64], for turbulent flows (generally $Re > 10^4$) can be determined as a function of the Reynolds number. The Reynolds number of the rotor was calculated as $Re = \frac{(w \cdot 2b)}{v}$ at each discretization step. In this way, a logarithmic law for n was

implemented as follows:

$$n = 0.7823 \cdot \ln(Re) - 2.0013 \quad (26)$$

When the Reynolds number is lower than $2 \cdot 10^3$, the laminar expression derived from [55] was adopted. When the Reynolds number is between $2 \cdot 10^3$ and 10^4 and thus corresponds to a transitional flow regime, a parabolic distribution with higher value of coefficient a can be used rather than a power law equation. Indeed, from a comparison of EES and CFD analyses performed in the same conditions (Table 2) as those reported in [29] with air working fluid, it was found that a parabolic distribution ensures a better matching of the results (Fig. 3). The best matching of results was achieved when a higher coefficient value of the parabolic distribution profile law was adopted for Reynolds number in the transitional field.

The CFD analyses were performed in order to determine the flow field within the discs of the Tesla turbine. For this purpose the commercial software ANSYS Fluent was utilized and three dimensional, double precision, pressure based, steady and implicit simulations were set. Velocity formulation was considered in the absolute frame and both laminar and transitional k-kl-omega models were analysed. The k-kl-omega was selected as turbulence model in order to evaluate the transitional behaviour of the flow, given that in this scheme transition is not fixed but triggered by velocity fluctuations in the boundary-layer. The pressure-velocity coupling scheme was set as SIMPLE, with second order upwind scheme for momentum and PRESTO! scheme for pressure equation. The geometry of the model was created with the software ICEM on a disc with outer diameter 125 mm, inlet diameter 32 mm and gap between discs of 0.1 mm. A real fluid model was considered for air, with Peng-Robinson scheme enabled.

A mesh sensitivity analysis was carried out for CFD simulations, using both laminar and k-kl-omega turbulence models. Several meshes were created, with the objective of investigating the effects of elements size and local refinement. In each case, the y^+ was selected to be lower than 1 for being able to evaluate transition effects when the suitable

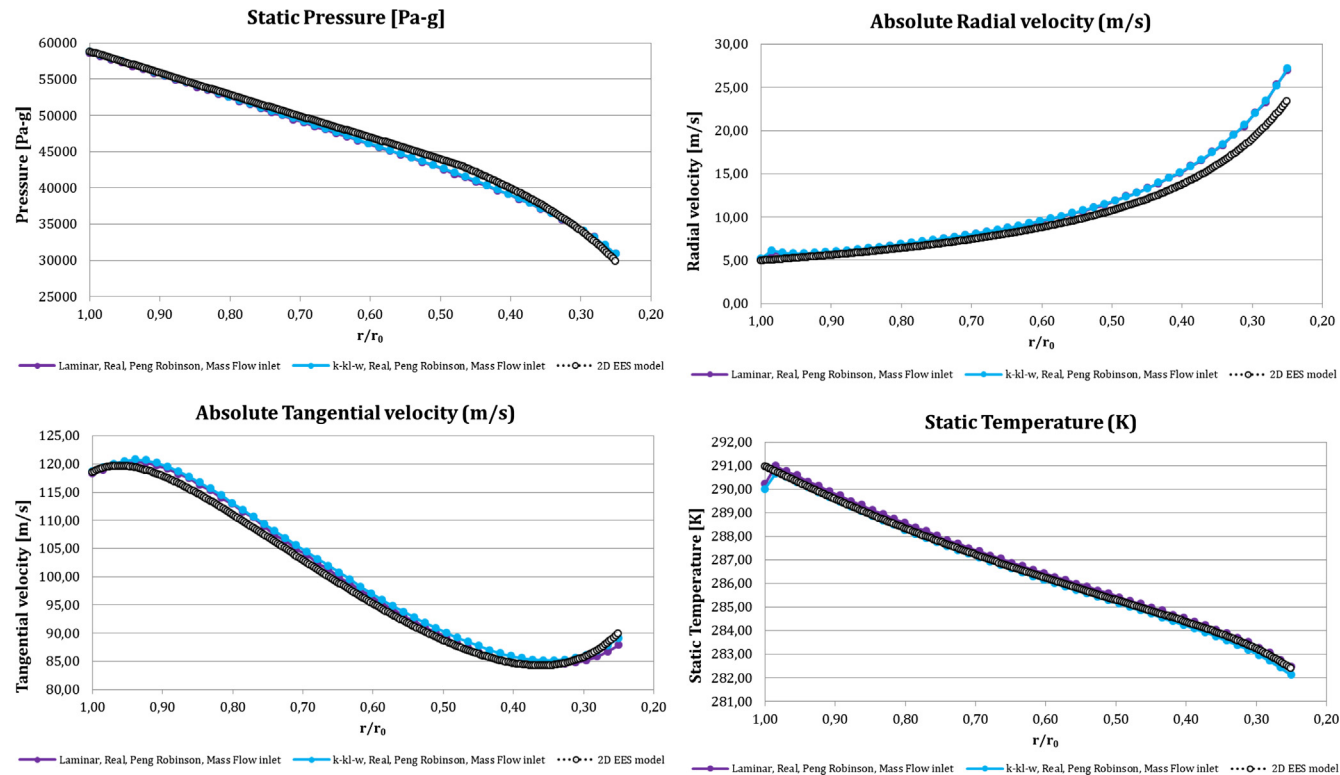


Fig. 3. Comparison between the results obtained with the EES and CFD analyses; (a) static pressure, (b) radial velocity, (c) tangential velocity, and (d) static temperature, along the radial direction.

turbulence model is applied; the mesh was refined in particular at inlet and near walls, where the laminar separation was expected to occur.

Tangential velocity was selected as parameter for mesh independence assessment, as this parameter proved to be the most affected by the grid characteristics, especially for transitional simulations (Fig. 2). In Fig. 2c it is noticeable that a mesh with at least 800,000 nodes ensures grid independence, while coarser meshes determine errors in absolute tangential velocity computation, both at inlet and at outlet.

In Fig. 3(a)–(d) the results of static pressure, absolute radial velocity, absolute tangential velocity and static temperature calculated with the EES model are compared with those computed with the CFD analyses carried out with a mesh made up of 3,125,000 nodes. The results obtained with the k-kl-omega model are very close to the ones achieved with the 2D home-built model.

The proposed rotor flow model has several relevant advantages: it is (i) accurate according to the comparison with CFD analyses; (ii) very flexible as a large number of velocity profile laws can be used; (iii) easily implementable in calculation software such as EES; and (iv) requires very reduced calculation time.

2.4. Stator/rotor coupling losses

The above presented stator and rotor models only take into account the distributed pressure losses inside the components, but they do not consider those concentrated into the stator–rotor gap. The passage of the flow from the throat of the nozzle to the gap and then to the rotor channel, involves an abrupt cross section enlargement followed by a contraction and generates large flow pressure losses. For an incompressible fluid, the concentrated pressure losses are calculated by the definition of a loss coefficient, depending on the system geometry and the flow conditions, which reduces the kinetic energy of the fluid [65]:

$$\Delta P_0 = k \cdot \frac{1}{2} \rho v^2 \quad (27)$$

For the case of Tesla turbine, it can be written as:

$$\Delta p = \Delta p_e + \Delta p_i = \frac{1}{2} k_e \rho v_1^2 + \frac{1}{2} k_i \rho w_1^2 \quad (28)$$

where Δp_e is the pressure loss occurring immediately after the throat section (abrupt enlargement) and Δp_i is the pressure loss related to the flow entering the rotor micro-channels (relative flow contraction) while k_e and k_i are their respective loss coefficients.

The loss coefficient for abrupt enlargement (k_e) was modelled as an incompressible Borda-Carnot coefficient [65], according to Eq. (30):

$$k_e = \left(1 - \frac{A_o}{A_i} \right)^2 \quad (29)$$

where A_o is the throat cross section, here having rectangular shape:

$$A_o = L_t \cdot H_s \quad (30)$$

The parameter A_i is the cross section on the disks (transversal) covered by the flow jet:

$$A_i = \left\{ \left[\frac{L_t}{\tan(\alpha_i)} + \frac{\text{GAP}}{\sin(\alpha_i)} \right] / \cos(\alpha_i) - \text{GAP} \cdot \tan(\alpha_i) - \frac{\text{GAP}}{\tan(\alpha_{PS})} \right\} \cdot H_s \quad (31)$$

Eq. (29) can be used for a turbulent flow with a uniform velocity profile; when these assumptions are not satisfied, some numerical and graphical correlations available in [65] can be used.

The total pressure loss for abrupt expansion can be calculated using the velocity immediately upstream the enlargement. A parametric analysis showed that the pressure loss is mainly influenced by the velocity v_1 (second order law), followed by the density and finally by the geometric parameters (throat width and gap extension).

The loss coefficient for abrupt contraction (k_i) was obtained through a polynomial fitting of empirical data, as reported in [65]:

$$k_i = -0.126 \left(\frac{A_i}{A_o} \right)^4 + 1.0296 \left(\frac{A_i}{A_o} \right)^3 - 1.279 \left(\frac{A_i}{A_o} \right)^2 - 0.1209 \left(\frac{A_i}{A_o} \right) + 0.5 \quad (32)$$

where A_o is the total cylindrical surface, including disks and channel surfaces:

$$A_o = 2\pi r_l \cdot H_s \quad (33)$$

While A_i only takes into account the cylindrical surface of the channel:

$$A_i = n_{ch} \cdot 2\pi r_l \cdot b \quad (34)$$

The velocity value utilized in this case is the radial component of the relative velocity w_{r1} (normal to passage section), immediately after the contraction. The main geometric parameters influencing the pressure loss are the height of the nozzle throat, the thickness and the number of rotor channels. Generally, the pressure loss for abrupt enlargement is far higher than the one for abrupt contraction at rotor inlet, because the velocity v_1 influencing the former is higher (typically by a factor 10).

Eq. (32) can be used if the flow Mach number is less than 0.3 so that the flow may be treated as incompressible, thus it is not applicable for the flow at nozzle output. To overcome this problem, an iterative calculation was implemented in order to achieve average values of density between the input and the output sections, allowing the recovery of compressibility effects.

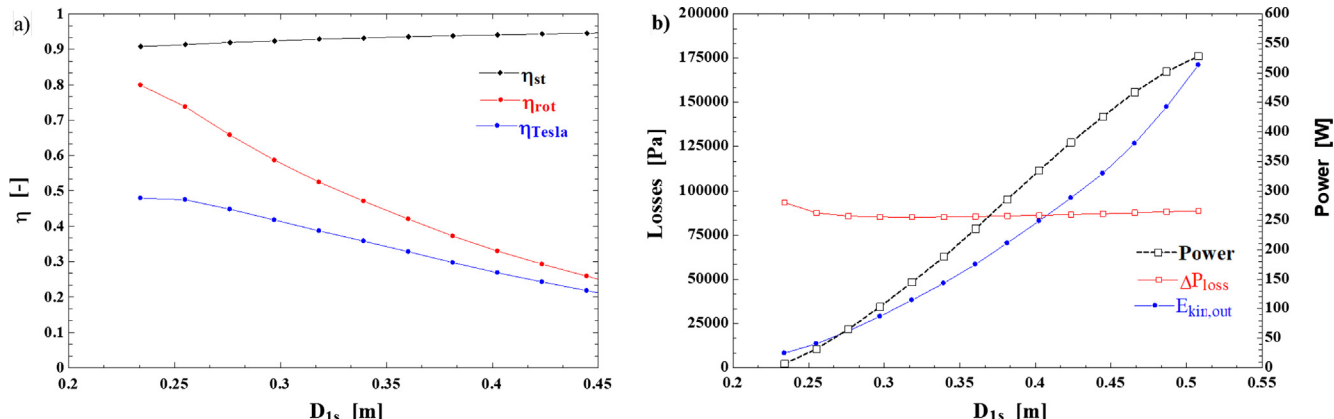


Fig. 4. Turbine efficiency (a) and turbine power and losses (b), versus rotor inlet diameters.

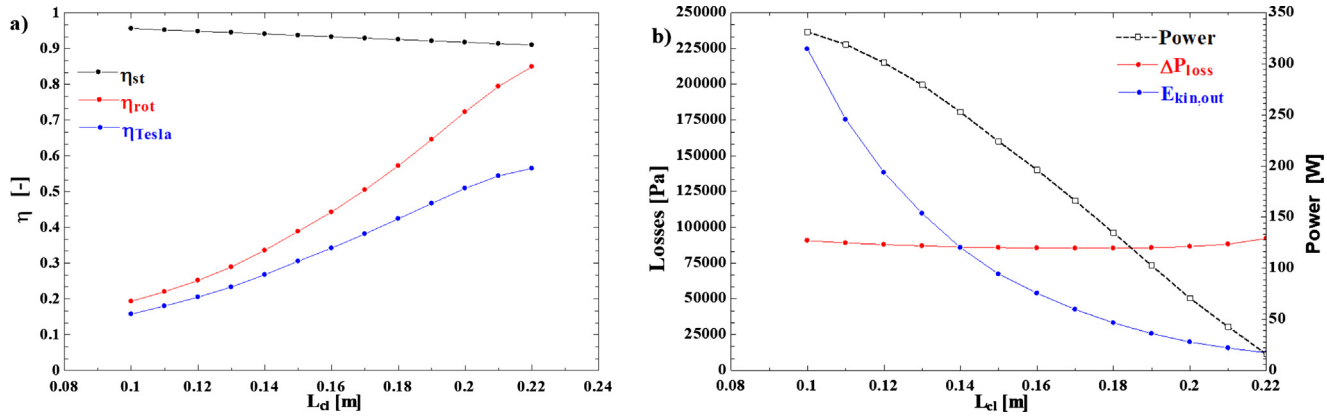


Fig. 5. Turbine efficiencies (a) and power and losses (b), versus length of nozzle camber line.

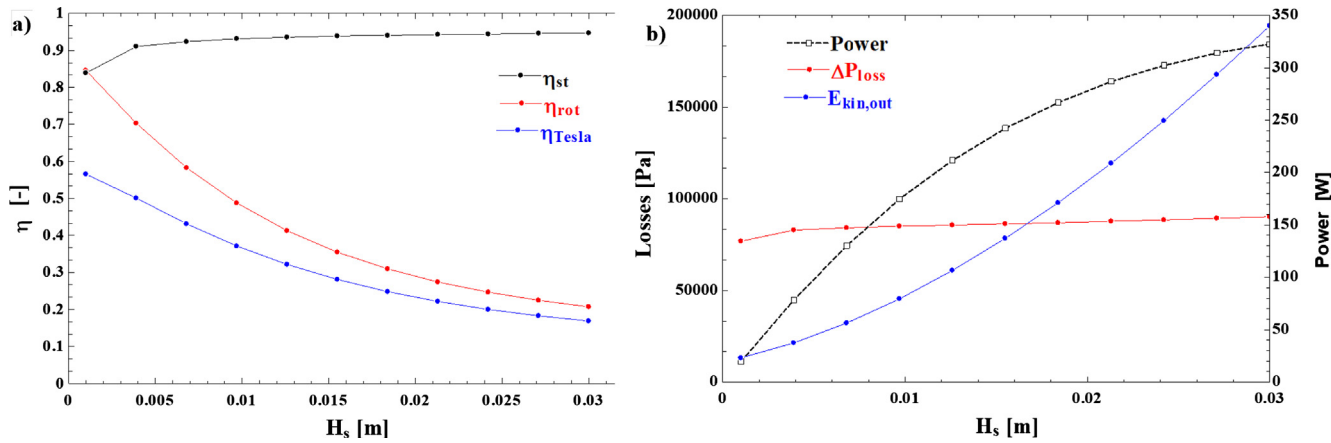


Fig. 6. Turbine efficiencies (a) and power and losses (b), versus height of the throat section.

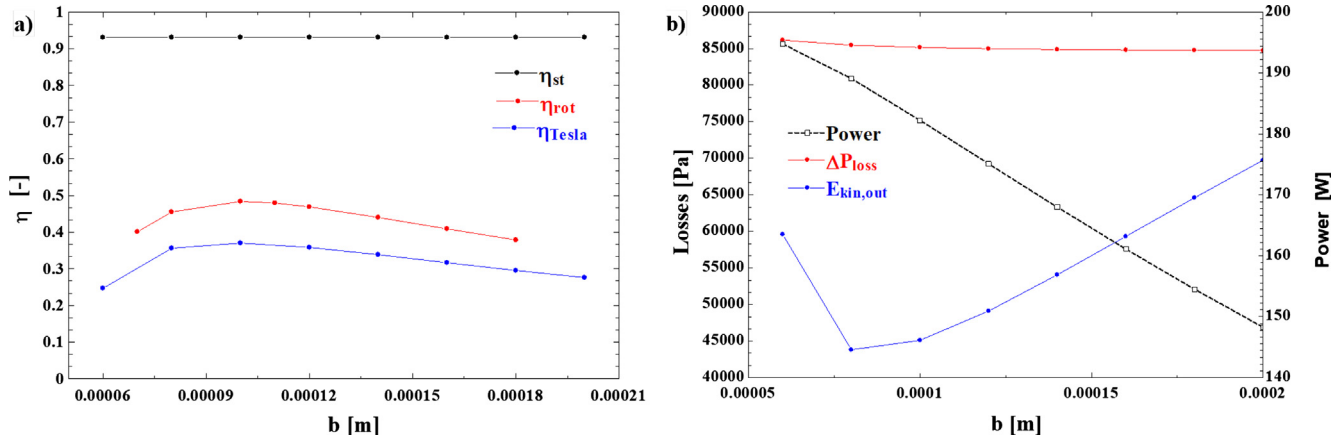


Fig. 7. Turbine efficiencies (a) and power and losses (b), versus disc channel height.

2.4.1. Joining the three models of the different flow zones of the expander

For the connection of the three different models of the developed flow (stator, rotor and gap pressure losses), the following assumptions were applied:

- Conservation of total enthalpy between the stator outlet and the rotor inlet, as the transformation may be considered adiabatic and without any work transfer.
- Invariable static enthalpy, and consequently constant absolute velocity v_1 while the flow direction changes during the gap crossing. It means that the pressure losses may be treated like an isenthalpic throttling process into a valve.

2.5. Model of the output diffuser

At the rotor outlet, the fluid trajectory is curved and the velocity mainly assumes an axial direction, while a consistent amount of kinetic energy is lost. The presence of a diffuser can partially recover these energy losses through a gradual section enlargement, which is able to decrease the fluid velocity, thus converting a fraction of the kinetic energy into pressure.

The model provides the calculation of the axial velocity at the diffuser inlet through the continuity equation, while the tangential and radial components are conserved from the rotor to the diffuser output. The continuity equation ensures the reduction of axial velocity due to

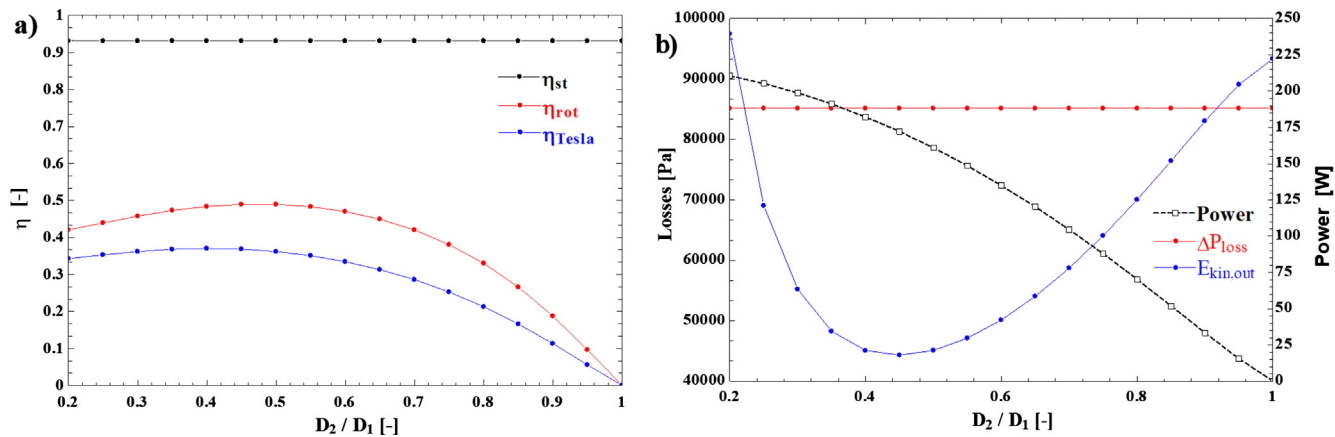


Fig. 8. Turbine efficiencies (a) and power and losses (b), versus in/out rotor diameters ratio.

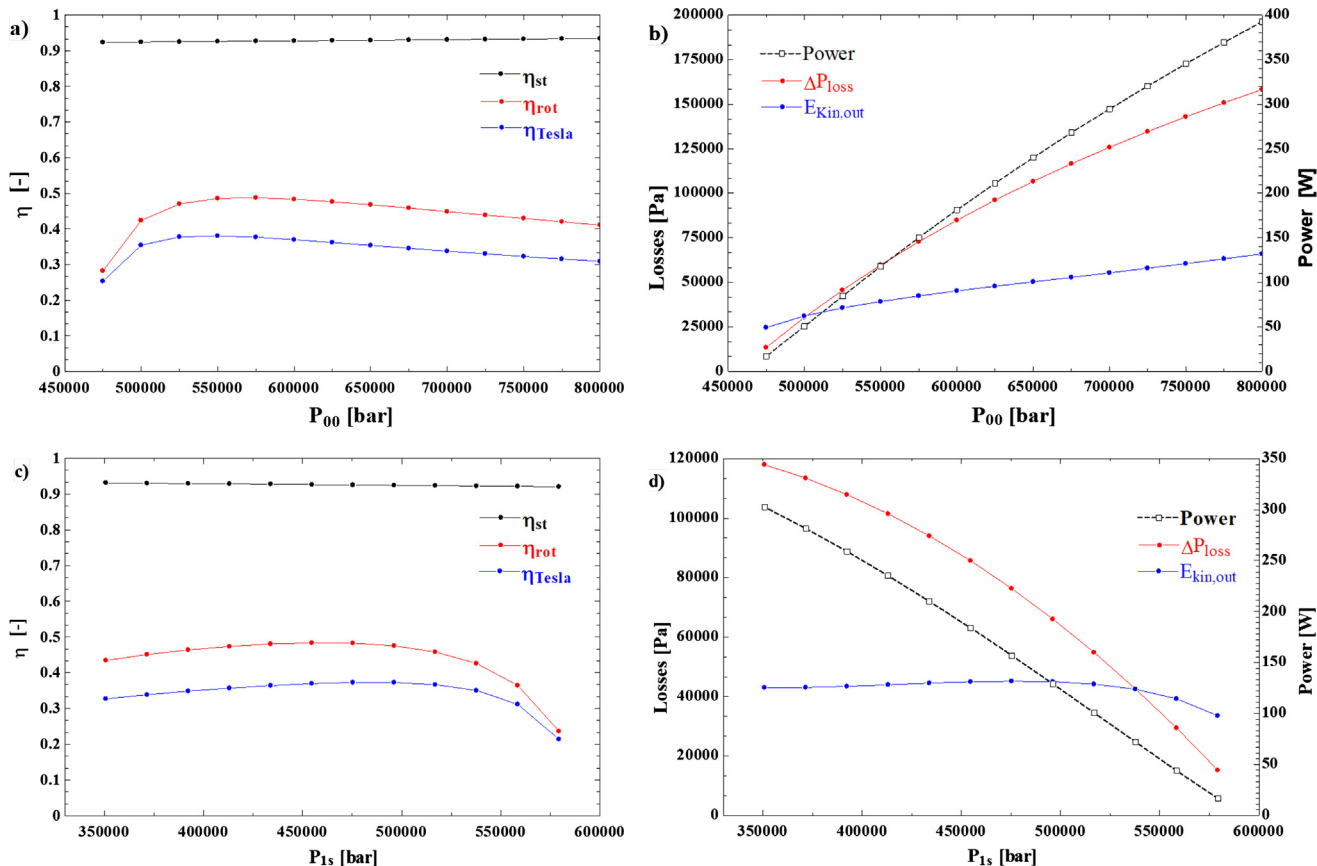


Fig. 9. Turbine efficiencies versus (a) Total inlet pressure, (c) Stator outlet static pressure and power and losses at various (b) Total inlet pressure; and (d) Stator outlet static pressure.

the increased section, while radial and tangential components were calculated by assuming the conservation of their angle with the axial velocity. These velocity components are responsible for a 3D swirled flow.

Inside the diffuser, the total enthalpy is conserved, while the total pressure is reduced due to the wall friction inside the diffuser:

$$P_{05} = P_{04} - k_{\text{diff}} \frac{1}{2} \rho_4 V_4^2 \quad (35)$$

This equation is similar to the one used for the abrupt enlargement, but the loss coefficient k_{diff} was obtained through a polynomial fitting of the experimental data available in [65] as a function of the diffuser in/out area ratio and the diffusion angle. A further step was the

assumption of swirled flow: in [66], a large number of diffusers were analysed and tested to evaluate the influence of vorticity on the performance, concluding that swirled flow could increase the diffuser efficiency. Therefore, an incremental coefficient, depending on the inlet/outlet area ratio of the diffuser, on the swirl ratio (i.e. the ratio between tangential and axial velocity), and on the diffuser angle, can be applied to the efficiency, defined as:

$$\eta_{\text{diff}} = \frac{P_5 - P_4}{\frac{1}{2} \rho_4 V_4^2} \cdot k_{\text{swirl}} \quad (36)$$

The pressure recovery and the outlet static pressure are increased due to the swirled flow.

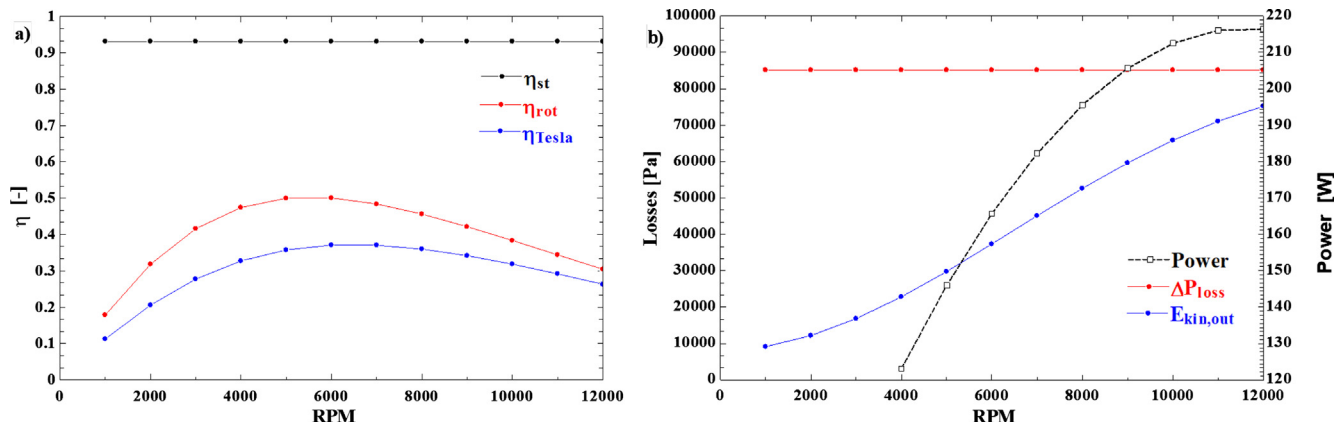


Fig. 10. Turbine efficiencies (a) power output and losses (b), versus rotational speed.

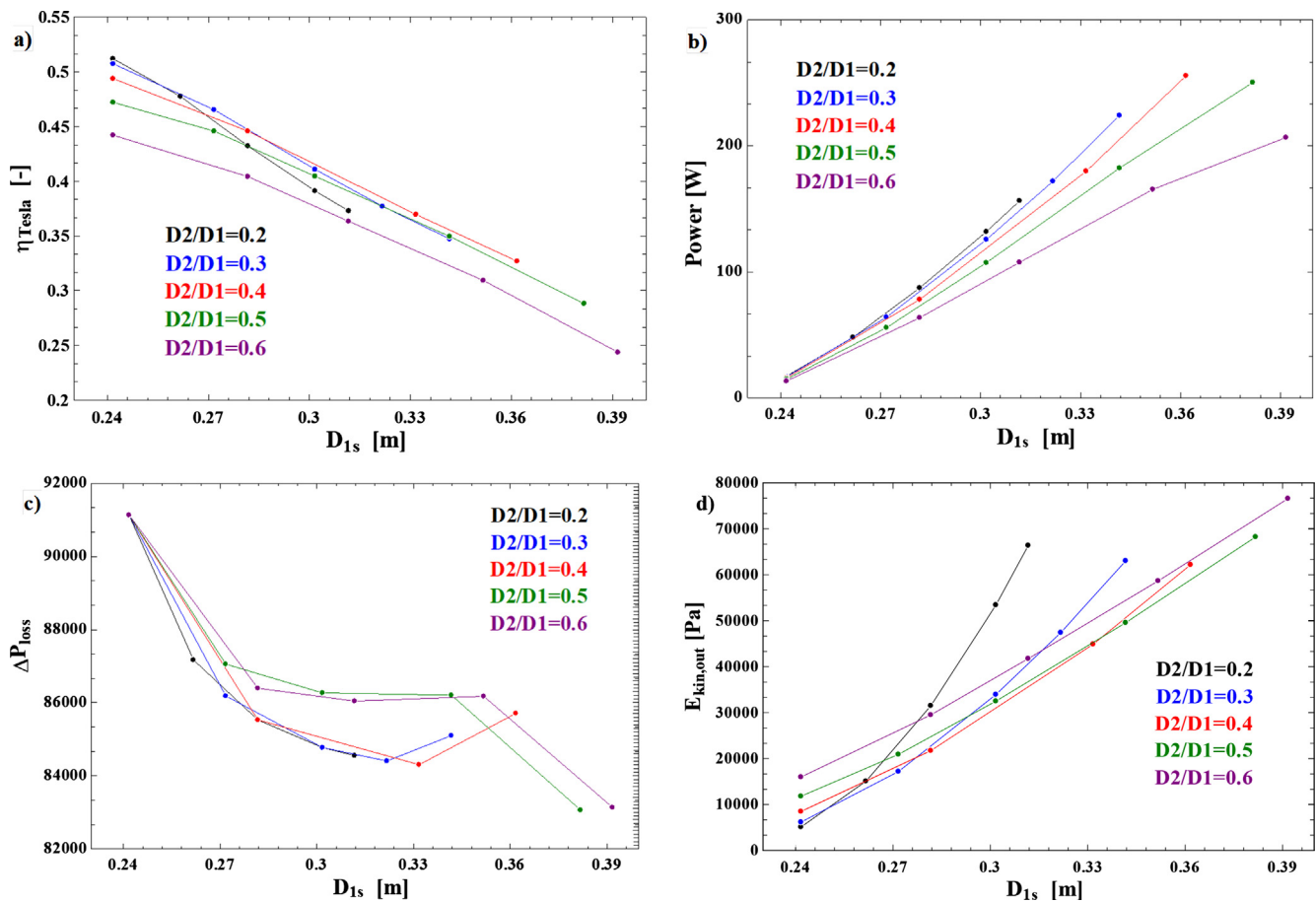


Fig. 11. Turbine efficiency (a), power output (b), between stator–rotor losses (c) and kinetic energy at rotor outlet (d) versus stator output diameter at variable in/out rotor diameter ratio.

3. Results

3.1. Parametric analysis

In order to assess the performance potential of the Tesla turbine, a parametric analysis was carried out: the performance parameters were evaluated as functions of the main geometric variables and operating conditions. The N-hexane was adopted as working fluid, due to its favourable low expansion ratio and the well suitable thermodynamic critical conditions (e.g. low critical pressure 3.034 MPa and high critical temperature 234.67 °C [67]). Furthermore, hydrocarbons are among the best compromises between environmental constraints (having zero

ODP and GWP and fairly low toxicity [67]), and good thermo dynamic cycle features for use in ORCs. The only drawback might be the flammability, but the rapidly increasing safety standards, coupled to typically small or micro sizes for which Tesla expander technology is generally conceived, make hydrocarbons particularly attractive for these applications.

3.2. Individual variables optimization

In this section, the influence of each single parameter on the performance of the turbine is analysed, while keeping constant all the other geometric and thermo dynamic parameters.

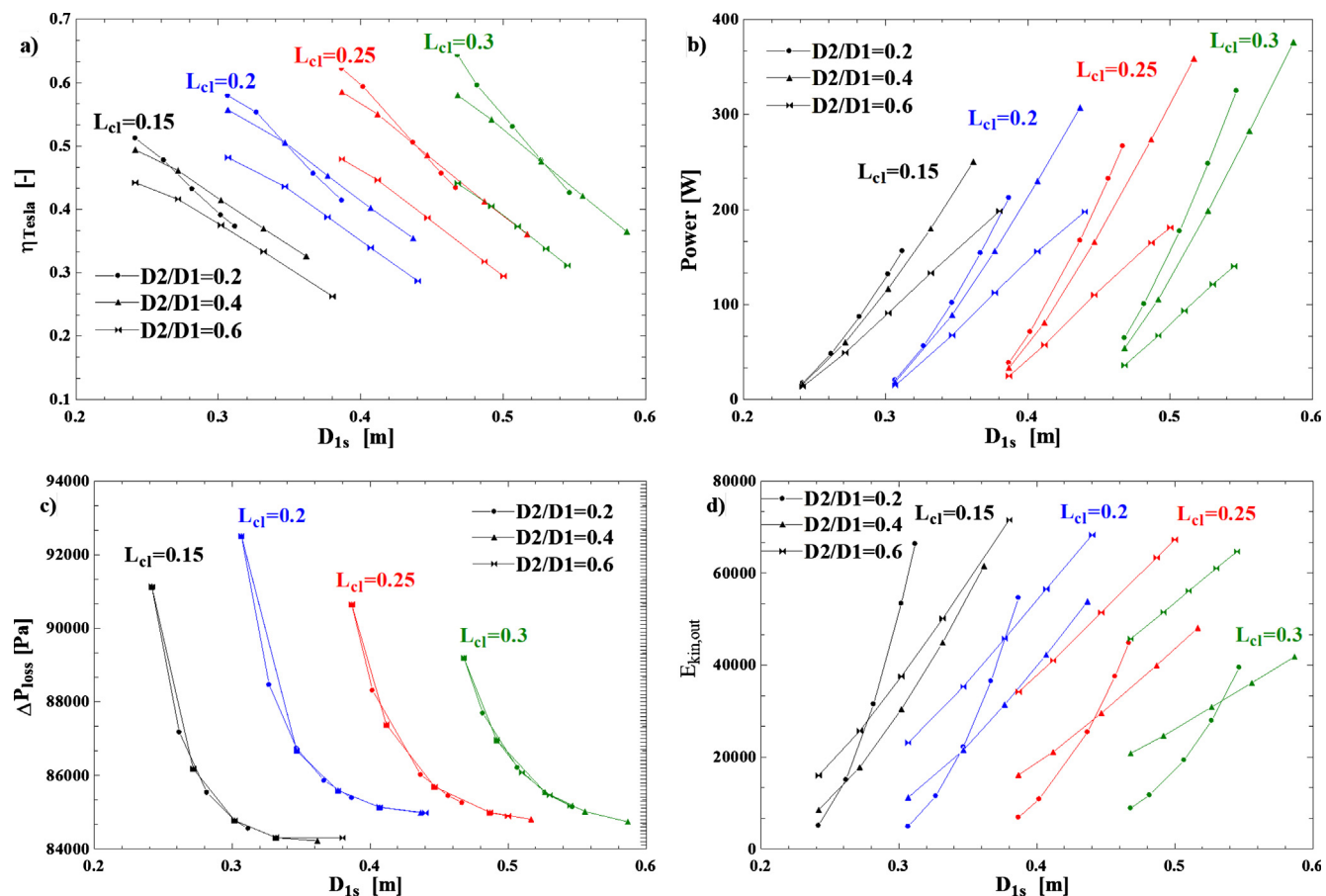


Fig. 12. Turbine efficiency (a), power output (b), stator-rotor losses (c), and kinetic energy at rotor output (d) versus stator exit diameter, for different rotor in/out diameter ratio and camber line length.

3.2.1. Rotor inlet diameter

The rotor inlet diameter is one of the most important parameters, because it plays a primary role on both the power output and the size of the machine. When fixed thermodynamic conditions and velocity are assumed at the stator output, a higher rotor diameter is associated to a larger throat section. Therefore, according to continuity equation, a higher mass flow rate is obtained. On the contrary, the increased expansion ratio is responsible for an increase of velocity at rotor outlet. It leads to higher kinetic energy losses, which become unbearable when the outlet Mach value overcomes the inlet one and, because this condition is not acceptable, the value of D_{1s} is limited. The work output per unit mass of the expander is defined by the Euler equation:

$$\text{work} = v_{t1} \cdot u_1 - v_{t2} \cdot u_2 \quad (37)$$

Since both the first and second terms increase with larger rotor diameter, the specific work output shows an optimization value, while the overall power output, mainly influenced by the mass flow rate, has a monotonically increasing trend. The rotor and total efficiencies are affected by increasing the rotor isentropic enthalpy drop, thus their values decrease, as shown in Fig. 4.

3.2.2. Camber line length

The length of the camber line in the stator channel is another parameter that influences turbine performance. An increase of the camber line, while keeping the other geometrical parameters fixed, is responsible for the reduction of the throat section width and, consequently, of the flow rate. The flow velocity at the rotor outlet decreases and generates a higher work output, according to Eq. (37). Therefore, an increase in the length of the camber line has the same effect of a reduction of the rotor inlet diameter (Fig. 5).

3.2.3. Height and width of the nozzle throat section

The height of the throat section only slightly affects the geometry and the variables at the stator output, including the mass flow rate, which shows a linear trend and varies in a reduced range. The maximum value is determined by the sonic condition at the throat section: decreasing the height of the rectangular area, the continuity equation ensures a reduced flow rate and, consequently, a lower expansion rate inside the rotor. The velocity components are both proportional to the flow rate (Eqs. (8)–(10)), so the Mach number increases rapidly, thus increasing the overall efficiency (Fig. 6).

The reduction of throat width is responsible for a more than linear decrement of flow rate and velocity at rotor outlet that results in a reduction of power output and kinetic energy losses at rotor exit, whereas the expander efficiency shows a linear increment.

3.2.4. Rotor channel height

The channel height, which is present in Eq. (10), is directly proportional to tangential velocity and inversely proportional to radial velocity. It leads to a maximization of the rotor outlet Mach number and, accordingly, to a minimization of outlet rotor pressure. This value of channel height corresponds to the one optimizing both rotor and turbine efficiency, as lower velocities are associated to lower kinetic energy losses (Fig. 7).

3.2.5. Outlet rotor diameter

The variation of D_2 shows an interesting minimum value of tangential velocity at rotor outlet, as a result of Eq. (10). As well as in the previous analysis, the value of in/out rotor diameter ratio D_2/D_1 is characterized by the minimum energy loss and, therefore, the maximum turbine efficiency (Fig. 8).

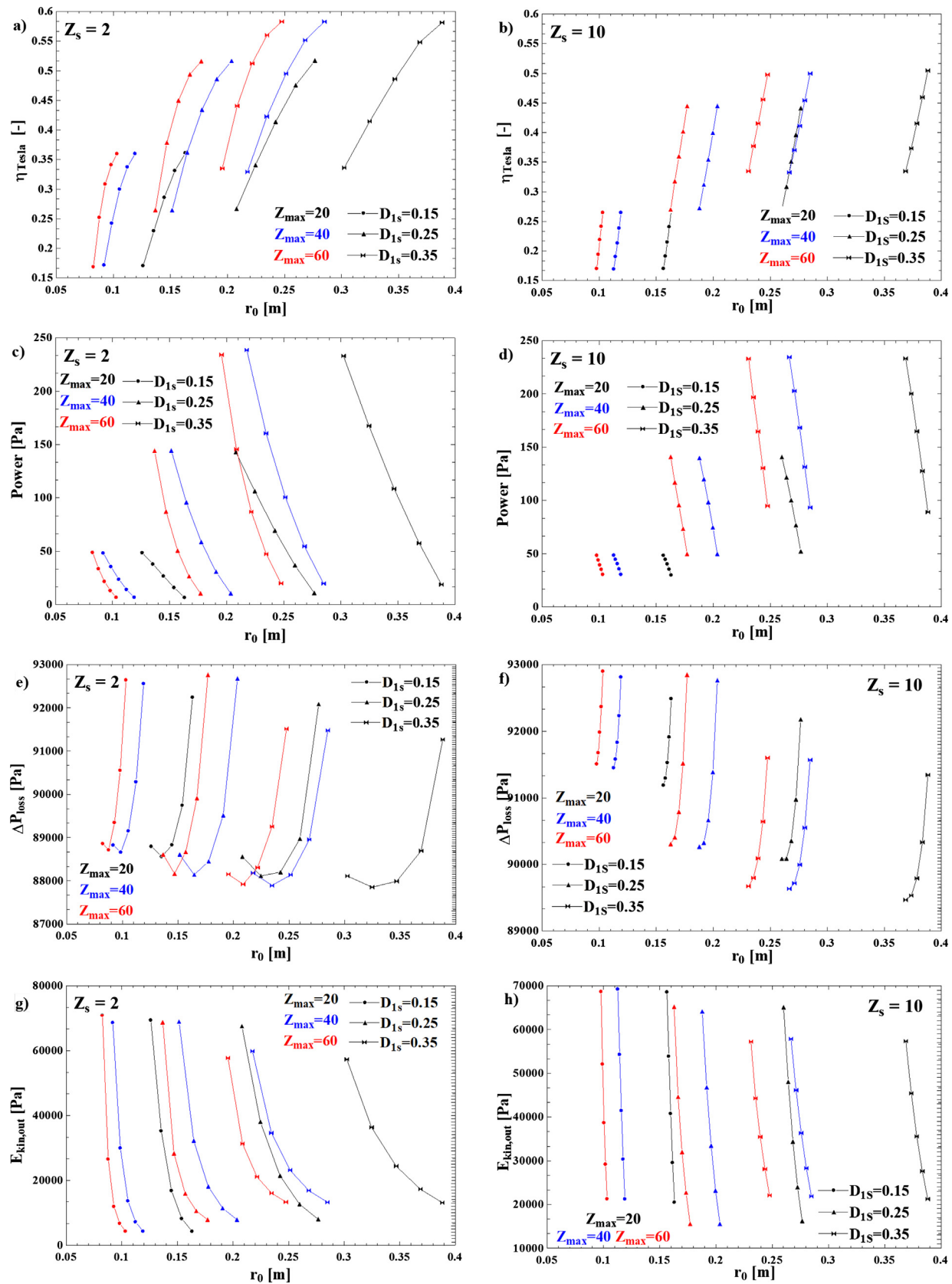


Fig. 13. Turbine efficiency, power, losses between stator and rotor, kinetic energy at rotor outlet at different stator inlet and exit diameters, with 2 nozzle channels (a, c, e, g) and 10 nozzle channels (b, d, f, h).

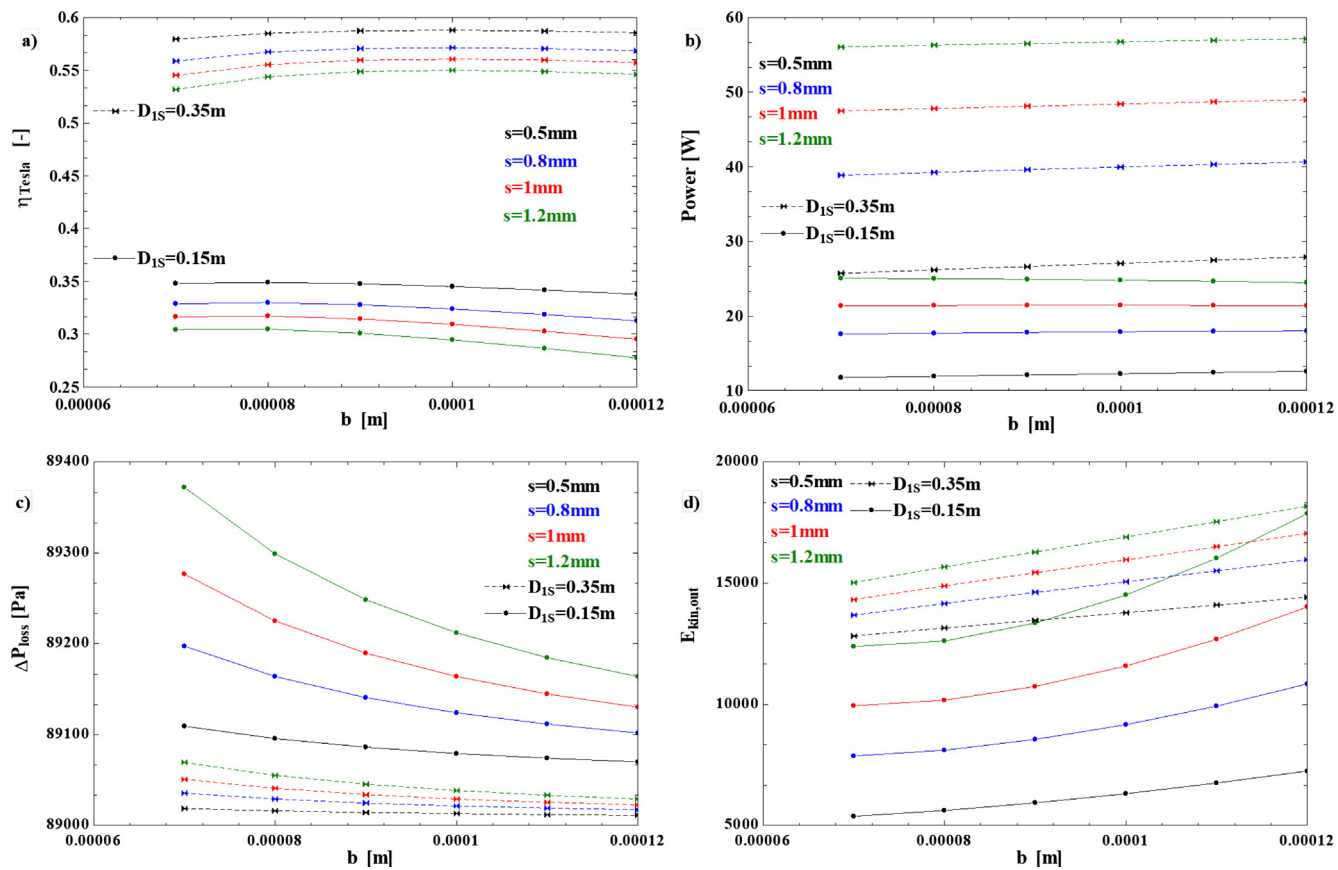


Fig. 14. Turbine efficiency (a), power output (b), stator–rotor losses (c), kinetic energy at rotor outlet (d) at various channel height b for different values of plates thickness s .

3.2.6. Thermodynamic conditions

The influence of the thermodynamic conditions on the turbine performance was considered; specifically, the total conditions at the stator inlet, for a fixed superheating level were evaluated. With increasing pressure, a higher flow rate is achieved (in spite of the higher temperature that partially reduces the fluid density) and subsequently a higher expansion rate, while the fluid heating generates higher values of output temperature T_2 . As reported in [30], there are conditions producing negative relative velocities at rotor inlet, then a flow reversal. Therefore, for a particular value of inlet total pressure P_{00} , the relative velocity becomes zero. In this condition, the rotor inlet radial velocity component V_{1R} has the minimum value and maximizes turbine efficiency (Fig. 9a and c).

The static pressure at the stator output determines the pressure range into the convergent channel and the mass flow rate. The effect of increasing P_{1S} is the same as a reduction of P_{00} , therefore an efficiency optimizing working point for the machine can be found (Fig. 9b and d).

3.2.7. Rotor peripheral speed

The variation of the rotor peripheral speed influences the relative tangential velocity w_{t1} , thus a value of peripheral speed above which a reversal flow condition is generated exists. At disc output, the pressure decreases when the rotational velocity is higher, because of momentum equilibrium in radial direction (as happens for pumps where $H \equiv \text{RPM}^2$). An efficiency optimising value of expander rotational speed was found between 4000 and 6000 rpm, as shown on Fig. 10. This first parametric study points out the close relationship between mass flow rate, rotor expansion ratio and turbine efficiency, confirming the statements claimed by Rice [26,23].

3.3. Combined variables

Considering the variation of each parameter individually is not enough for achieving a full optimization procedure because of their mutual influence. The combined variation of the inner and outer disc diameter shows an improvement of the expander efficiency (η_{Tesla}) at reduced values of stator outlet diameter D_{1S} and rotor outlet diameter D_2 . It is due to the reduction of the mass flow rate, whereas the power output has an opposite behaviour (see Fig. 11).

A more complete assessment was achieved taking into account the influence of the diameters of the whole turbine parts. It was done by adding a further parameter to the previous ones, namely the camber line length, which is correlated to the external radius. Again, the efficiency is maximised when the throat section is at the minimum value, but it can also be pointed out that long camber lines give better results when coupled with low D_2/D_1 (Fig. 12). These conditions allow the achievement of relatively high overall turbine efficiency (64%).

A comprehensive study of the stator should also include the camber line length, the throat length and the actual number of channels. The curves in Fig. 13 show that the best conditions are achieved for larger turbine extensions (r_0 and D_{1S}), as this allows a reduction of throat section and mass flow rate. However, Fig. 13 shows that for a fixed external 0.35 m diameter, the maximum efficiency can be kept constant by reducing both the external radius (larger turbine size), and the length of the camber line. As discussed, this is due to the counter-balancing effects, which maintain the mass flow rate constant. In this way, a Tesla turbine may achieve a more compact shape and the throat length can be reduced. A higher number of stator channels (Z_s in Fig. 13) is responsible for steeper curves and lower global efficiency at fixed values of r_0 and Z_{\max} .

The analysis of the nozzle throat height can be done if also the rotor

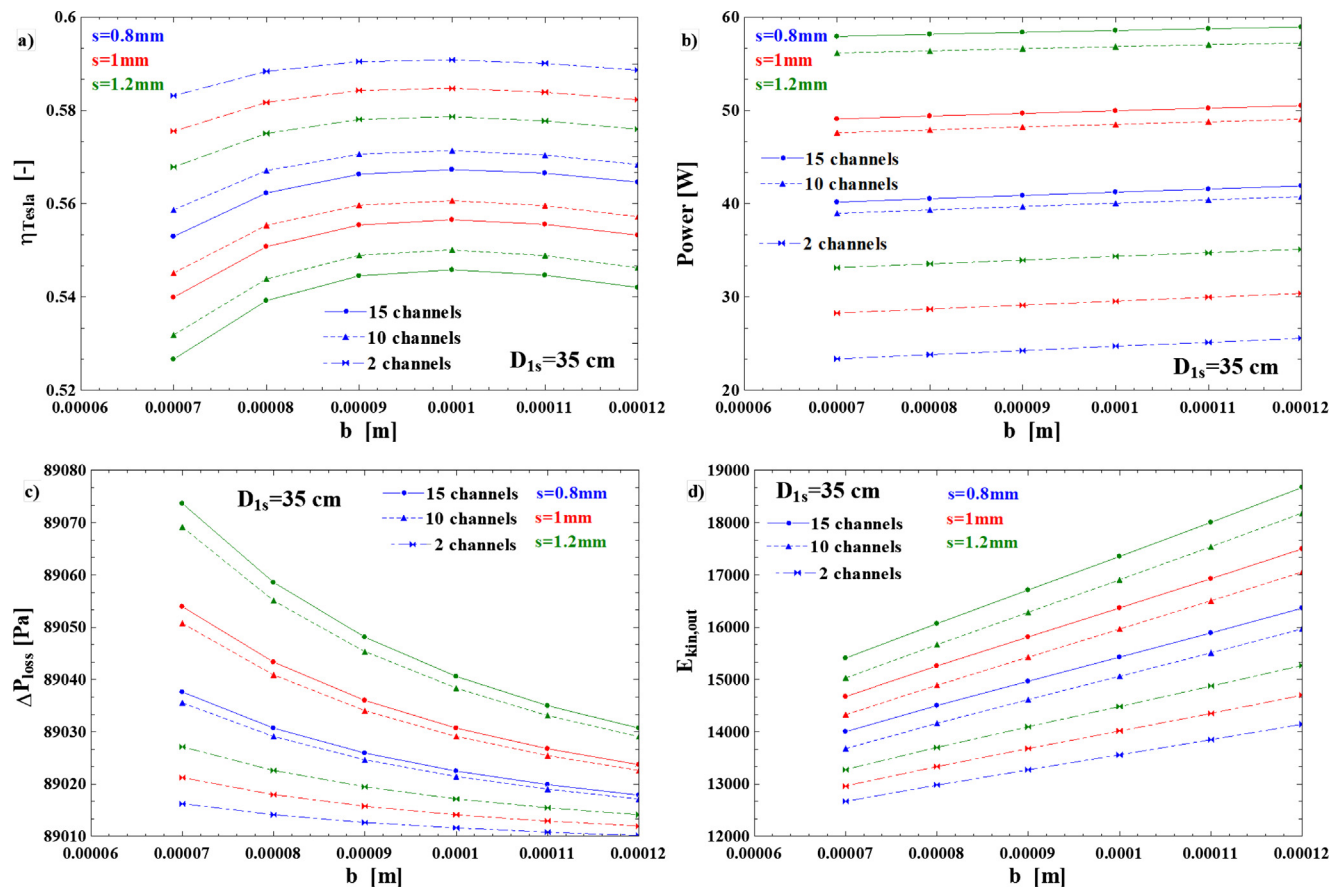


Fig. 15. Turbine efficiency (a), power output (b), stator – rotor losses (c), kinetic energy at rotor outlet (d) at various plates thickness s for different channel heights b and three configurations with different total number of channels.

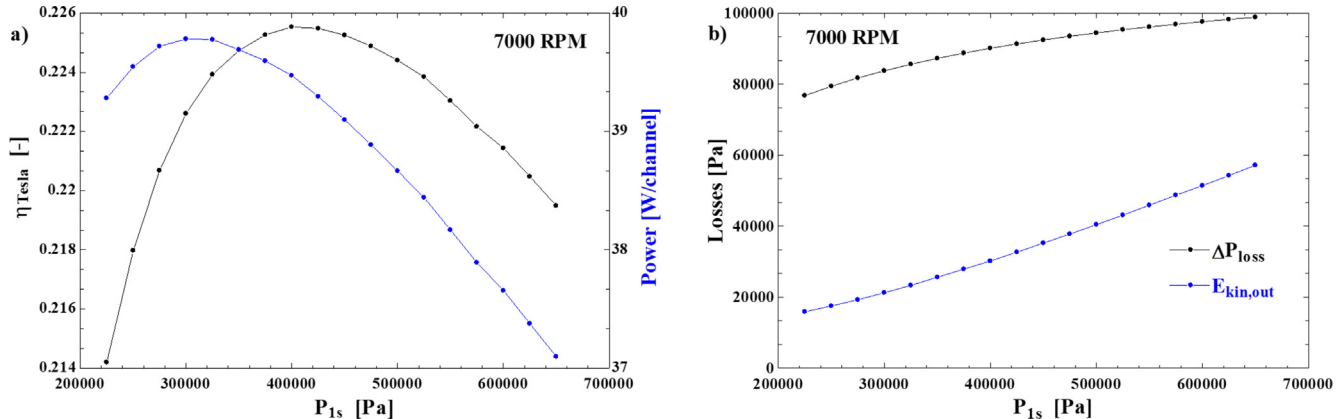


Fig. 16. Turbine efficiency and power output (a) and losses (b) versus static pressure at stator outlet ($D_{1s} = 0.15$ [m]).

channels height b and the thickness of the discs s are considered. The study was performed using a constant value of throat length ($L_{ts} = 1$ mm) and 10 channels in the rotor. The minimum values of b and s were chosen taking into account potential manufacturing and structural issues. The curves show a turbine efficiency optimizing value of b for both the assessed rotor diameters (0.8 mm for $D_{1s} = 15$ cm and 1 mm for $D_{1s} = 35$ respectively), while the increase of discs thickness is responsible for a wider throat section and a higher flow rate (higher power output), which entail a reduction of turbine efficiency η (Fig. 14).

The variation of the number of rotor channels (and consequently H_s) does not affect the behaviour of the curves and the optimising value of b , although a reduction in the number of rotor channels n_{channel} can

sharply improve the overall efficiency of the turbine (Fig. 15). The use of just 2 channels for every module allows to reach efficiency values (η) near 60%, also reducing the influence of the discs thickness. On the other hand, the reduction in number of channels implies a drop of power output, which can be counterbalanced by utilizing a higher number of modules.

The result of the above sensitivity analysis drove to an optimized and balanced design of the Tesla turbine, which may be summarised in the following:

- **Stator**, 4 convergent nozzles with a squared throat section (1×1 mm);
- **Rotor**, 10 channels 0.1 mm wide each; discs diameters ratio 0.4; the

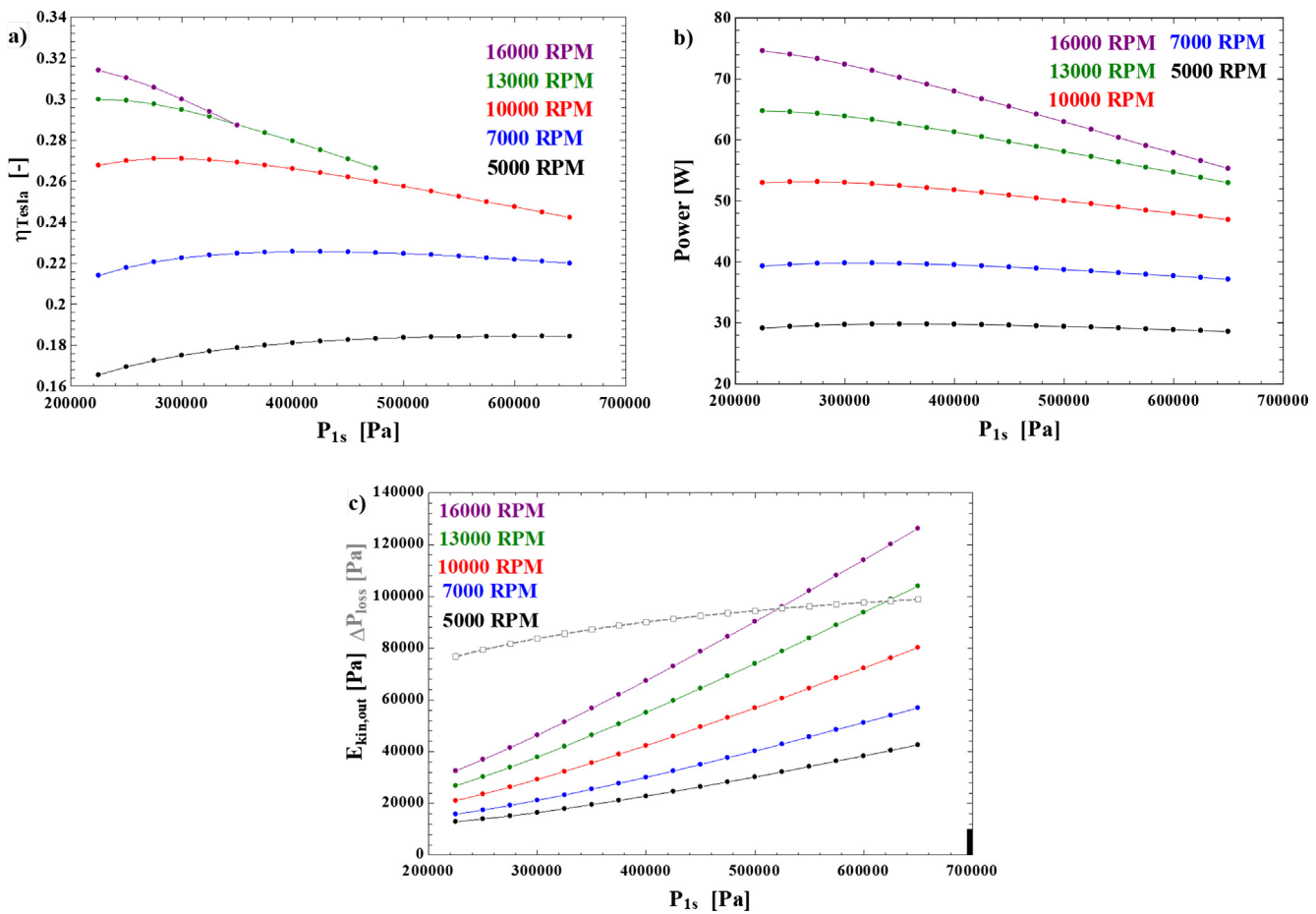


Fig. 17. Turbine efficiency (a), power output (b), and losses (c) versus static pressure at stator outlet for variable rotational speed ($D_{1s} = 0.15 \text{ m}$).

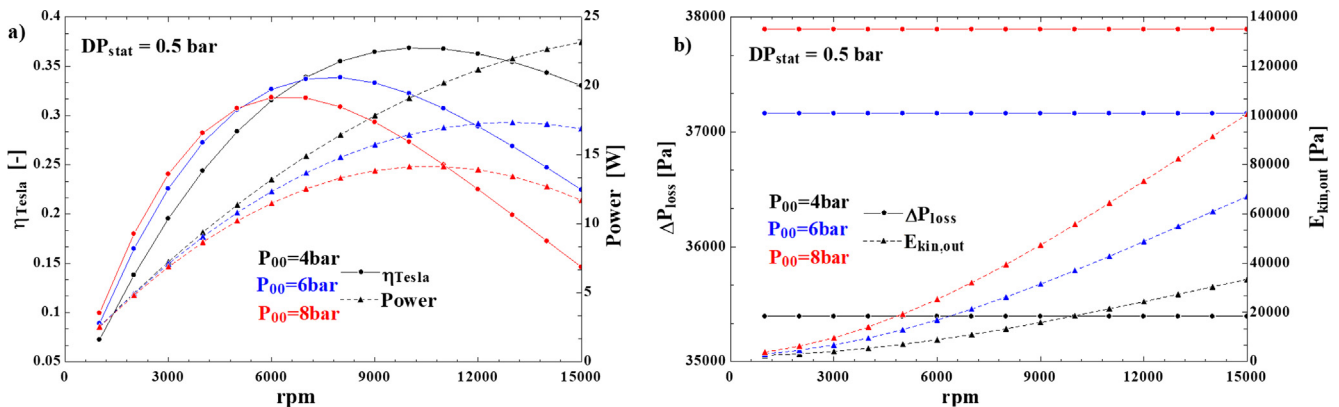


Fig. 18. Turbine efficiency and power output (a), losses (b) versus rotational speed at variable stator static pressure drop ($D_{1s} = 0.15 \text{ [m]}$).

external radius was not fixed, in order to evaluate the effects of the turbine size.

Finally, with the above-defined geometric design, the sensitivity analysis to the variable expander operating conditions was carried out. At the beginning, the superheating temperature and the pressure drop ΔP inside the stator were fixed: the minimum value of total pressure P_{00} and total temperature T_{00} were set, in order to avoid the sonic condition at the stator outlet. An optimal value of P_{1s} was found, as the turbine efficiency is strongly affected both by the mass flow rate and the enthalpy of the fluid: the former decreases with reducing P_{00} (leading to a positive effect on the turbine efficiency η), whereas the latter has the same effect of T_{00} (positive when the temperature increases). The same

considerations can be extended to the power output, which shows an optimizing value at lower total inlet pressure, due to the increasing density and mass flow rate (Fig. 16).

The sensitivity analysis to the rotational velocity showed that the expander efficiency η increases at higher speeds, with a slight peak placed at lower pressure (the limited extension of the curve at higher RPM is due to the high Mach number reached at the rotor outlet, Fig. 17).

In Fig. 18 are shown the expander efficiency and the power output to the change of the rotational speed at variable stator inlet total pressure P_{00} : an optimising value of rpm is present, lower at higher total inlet pressure; the efficiency increases at lower P_{00} , due to higher u and lower v_{t2} , which imply higher work output. The presence of a maximum

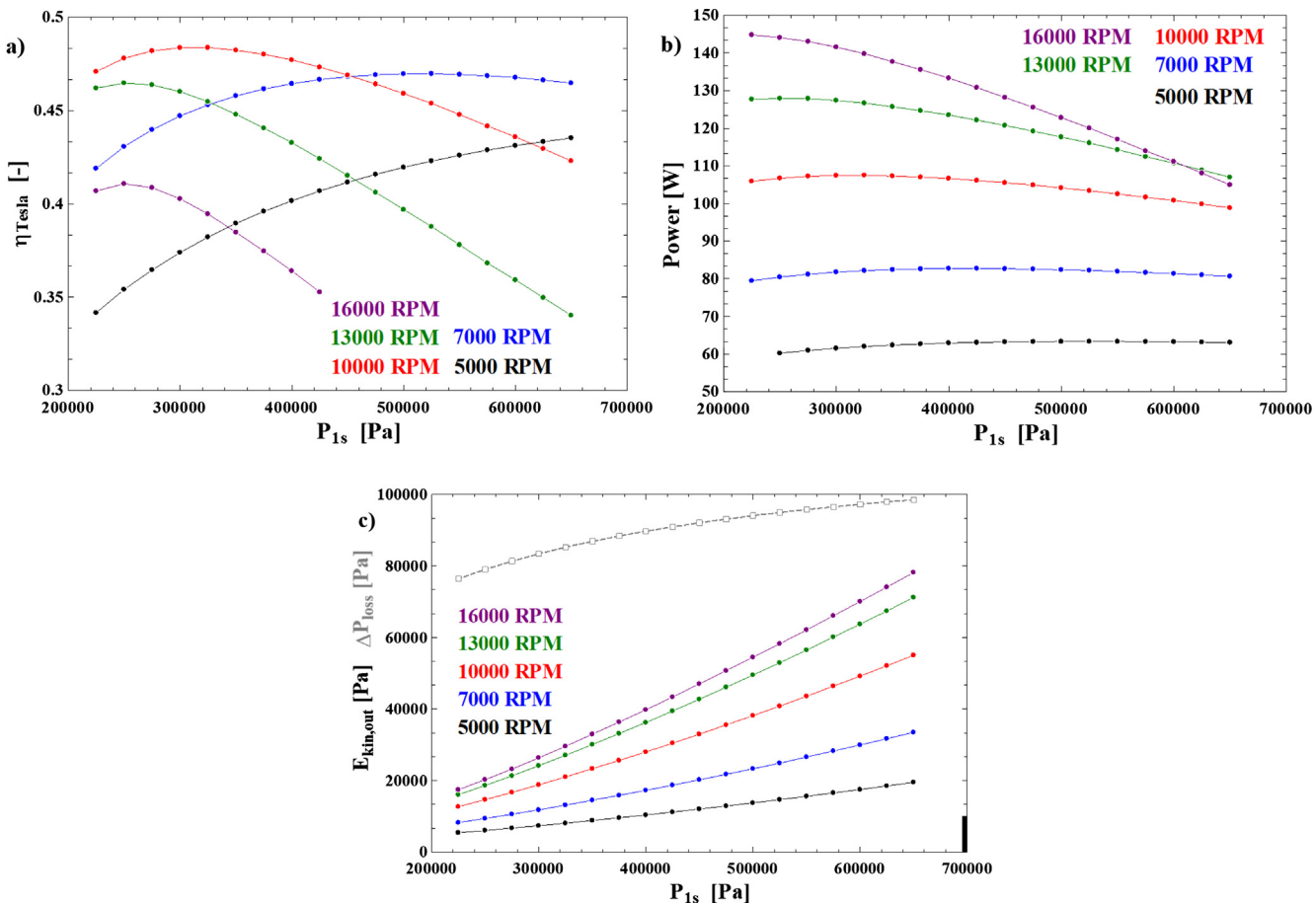


Fig. 19. Turbine efficiency (a), power output (b) and losses (c) versus static pressure at stator output, at variable rotational speed for the up-scaled expander ($D_{1s} = 0.3$ m).

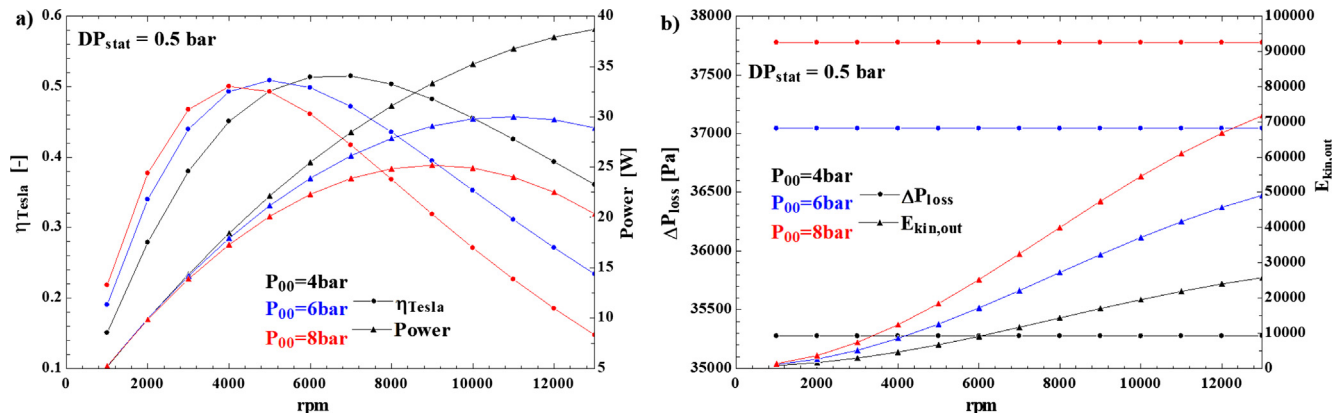


Fig. 20. Turbine (a) efficiency and power output, (b) losses versus rotational speed rpm at various total inlet pressure, for the up-scaled ($D_{1s} = 0.3$ [m]) expander.

can be explained by the momentum balance: a higher velocity increases the work output, but, at the same time, also the expansion ratio and the enthalpy drop through the rotor are enhanced. In this way, from the definition of total to static efficiency $\eta = \frac{\text{work}}{h_{00} - h_2}$ the presence an optimizing value comes out.

The superheating temperature level has a weak influence on the turbine efficiency η compared to pressure and rotational speed.

When up-scaling the Tesla expander size (for example doubling the diameter), while keeping the in/out rotor diameters ratio and throat section wide fixed, the performance curves show a very similar behaviour to the previous ones (Fig. 17) but with improved values (Figs. 19 and 20). The efficiency of the expander has an optimizing value of P_{1s}

and rotational speed (3.3 bar and 10,000 rpm respectively).

Finally, a very small ΔP_{stat} (in this case 0.5 bar) allows the reduction of inlet total pressure, optimising rotational speed and, on the whole, an increase of the turbine efficiency η up to 51%.

Following the above sensitivity analysis, it was possible to summarize the guidelines for design and optimization of a Tesla turbine working with N-hexane:

- The expander efficiency, power output, mass flow rate and expansion ratio are in close relation: low mass flow rates in are connected to high efficiency and lower power output and vice versa, in agreement to [26,23].

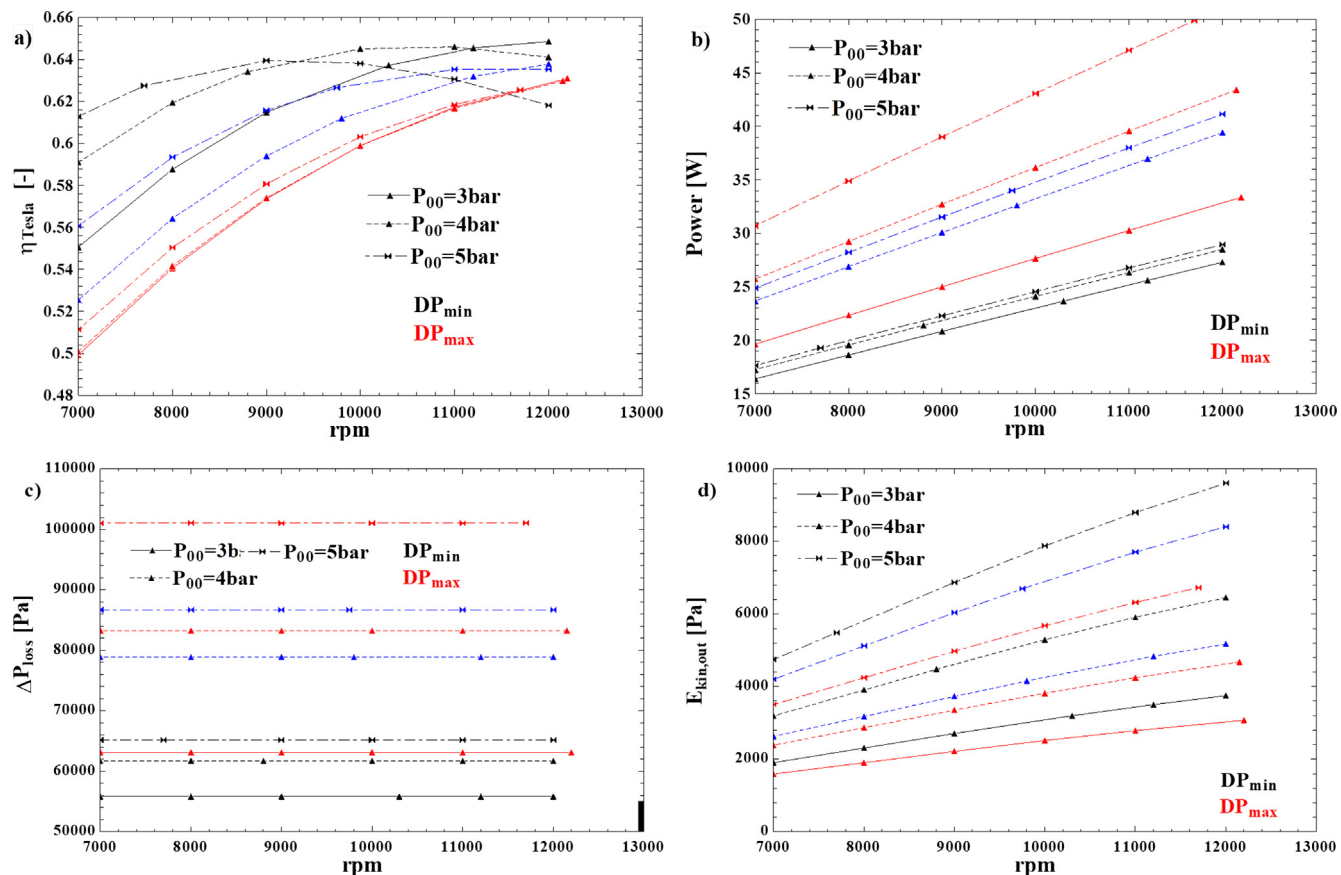


Fig. 21. Operating map of the Tesla expander: (a) efficiency, (b) power output, (c) stator-rotor losses, (d) kinetic energy at rotor outlet versus rotational speed at variable static pressure drop in the stator and total inlet pressure.

- The length of the camber line L_{cl} and the number of the nozzles Z are fundamental geometric parameters, as they directly influence the mass flow rate, while the rotor variables (b and D_2/D_1) influence the variation of tangential velocity Δv_t . They can be optimized in order to achieve the optimal performance.
- Generally, the best performance of the Tesla expander is achieved with low inlet pressure and mass flow rate. Under these conditions, an optimizing value of rotational speed is present. The performance is not significantly affected by inlet temperature.

3.4. Full design procedure

In order to achieve a complete and proper design, some boundaries to the geometric parameters must be fixed:

- Balanced stator size ($D_0/D_1 \leq 1.5$);
- Stator output angle $\alpha \leq 85^\circ$;
- Throat section length ≥ 1 mm;
- Rotor channel width ≥ 0.5 mm and discs thickness ≥ 1 mm.

Even the fluid conditions have constraints:

- $Ma_1 \leq 1$ in the throat section and $Ma_2 < Ma_1$.

By applying the discussed criteria and choosing discs with an external diameter $D_1 = 0.30$ m, the best efficiencies were achieved with a reduced throat section length (1 mm) and few statoric nozzles ($Z = 2$). On the other hand, this choice implies a low power output level and a non uniform flow at the rotor inlet. Under these conditions, the shape and the length of the statoric channels require an in/out diameter ratio D_0/D_1 equal to 1.48 while the need of a tangential flow is favoured by a

relatively large stator outlet angle d . The parametric analysis suggested $b = 0.12$ mm and $s = 0.5$ mm as the optimum rotoric channel width and disks thickness respectively, in order to maximize turbine efficiency. In this way, if the rotor is made of 5 discs, the throat section height is 2.6 mm, while the diameter ratio is set to 0.2.

Furthermore, a parametric study was carried out by varying P_{00} , P_{1s} and the rotational velocity. The efficiency was maximised at very low inlet pressure (4 bar) and stator pressure drop (0.5 bar), at 10,000 rpm rotational speed. Nevertheless, these operating conditions correspond to the incipient flow reversal at rotor inlet. This occurrence sets a limit on the values of rpm and ΔP_{stat} which, therefore, actually reduce the operating range. Nonetheless, very close values of efficiency can be achieved with lower inlet total pressure (3 bar) at higher rpm (Fig. 21).

The curves show that the maximum achievable value of efficiency is about 64%, possible at different combinations of total inlet pressure and rotational speed. In particular, raising the total inlet pressure allows lower rotational velocities in order to achieve the same efficiency levels. The effects of the inlet temperature are not very relevant and the efficiency is roughly constant versus temperature (Fig. 22). The modest variation is only due to the higher pressure losses in the gap between stator and rotor.

This study allowed the setup of a procedure to assess the correct design of an ORC Tesla expander, with the objective of achieving the highest possible performance.

In the present case, an inlet 5 bar total pressure and the related saturation temperature are the optimising conditions, while the ΔP_{stat} should be set at the value allowing the sonic condition in the throat section. The rotational speed showed an optimizing value at 11,700 rpm, which is the limit to avoid the reversal flow condition in the rotor. Under these design conditions, the Tesla expander achieved 54 W power output per channel and 61% isentropic efficiency.

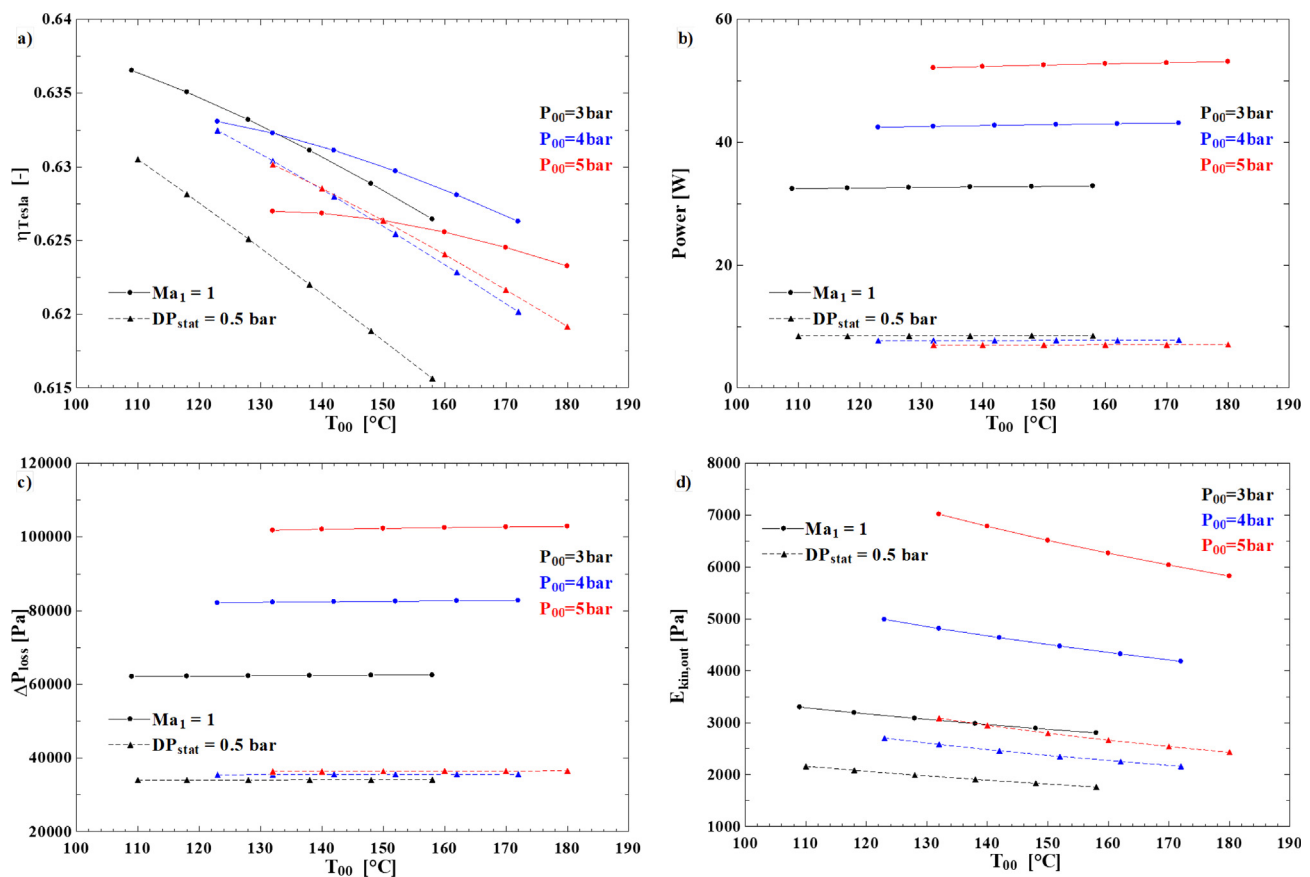


Fig. 22. Tesla expander Operating map: (a) efficiency, (b) power output, (c) losses stator–rotor, (d) kinetic energy at rotor outlet versus inlet total temperature at different total inlet pressure.

Table 3
Performance and geometric parameters of the assessed turbines.

	0.15	0.3	0.5
D_{1S} [m]	0.15	0.3	0.5
L_{ts} [mm]	1	1	1
H_s [mm]	1.2	1.2	1.2
Z_s [-]	2	2	2
b [mm]	0.1	0.1	0.1
D_2/D_1 [-]	0.25	0.25	0.25
RPM	23,400	11,700	7000
Φ	0.03	0.02	0.01
Ψ	0.86	0.92	0.93
N_s	0.029	0.013	0.008
D_s	9.07	80.08	34.16
n_{ch}	122	92	86
$\eta_{Tesla\ MAX}$ [%]	52	61	64
Power per channel [W]	41	54	58

Down-scaling or up-scaling the Tesla turbine by modifying the outer stator diameter D_{1S} , while maintaining the other main design parameters in the range suggested by the here proposed analysis, did not change the turbine performance appreciably (Table 3). Therefore, the proposed methodology and calculation model allows the optimised design of a wide size range of Tesla expanders for different possible mini/micro ORC applications.

4. Conclusions

A full design and optimization procedure for a Tesla expander was carried out by evaluating the performance of a specifically designed turbine working with N-hexane. A pivotal point of this research was the innovative design procedure of the expander compared to the current literature: it did not only consider the rotor or the stator separately, but

also included all the assembled components together, from the plenum chamber to the diffuser, passing through the definition of the stator and the rotor. The key outcomes of the present work may be summarised as follows:

- A novel methodology for the complete design of a Tesla turbine was proposed and assessed. Each component was designed taking into account the mutual relationships between the different parts of the machine.
- An innovative model for the solution of the rotor flow field was developed. Starting from an existing literature approach [29], the new one was generalized, considering the real fluid behaviour and the influence of the Reynolds number on the velocity profile inside the rotor channels.
- A sensitivity analysis to each geometric and thermos dynamic parameter was done. It was found that performance, mass flow rate and expansion ratio are strictly connected: low mass flow rates allow better efficiency and lower power output, in agreement to [26,23]. Furthermore, the best performances were achieved at low inlet pressure and optimal value of rotational speed, which is different for power output and efficiency. Generally, the inlet temperature has a minor influence on the performance. The right choice of channel height and in/out rotor diameter ratio is of primary importance in optimization of the expander efficiency.
- As an outcome of the developed model, three different design configurations of the proposed Tesla turbine were finally assessed. They achieved a total to static efficiency between 52% (in lower size version) and 64% (in larger size version). A power output of 58 W per channel was achieved with a 0.5 m diameter expander, which guarantees a very limited axial size of the turbine, thus resulting into a flat shape. Furthermore, up-scaling the turbine guarantees lower

rotational speed required to achieve the optimal design point.

As a final remark, the here conducted analysis showed how the complete assessment of a Tesla turbine needs to take into account not only the rotor model, which is the main part discussed in literature, but also all the other components of the expander and their interactions. For this reason, the present research might represent a complete and general methodology to assess the design and performance of a Tesla turbine.

References

- [1] Invernizzi C, Iora P, Silva P. Bottoming micro-Rankine cycles for micro-gas turbines. *Appl Therm Eng* 2007;27:100–10.
- [2] Chacartegui R, Sánchez D, Muñoz JM, Sánchez T. Alternative ORC bottoming cycles for combined cycle power plants. *Appl Energy* 2009;86:2162–70.
- [3] Al-Sulaiman FA, Dincer I, Hamdullahpur F. Exergy analysis of an integrated solid oxide fuel cell and organic Rankine cycle for cooling, heating and power production. *J Power Sour* 2010;195:2346–54.
- [4] Vaja I, Gambarotta A. Internal Combustion Engine (ICE) bottoming with Organic Rankine Cycles (ORCs). *Energy* 2010;35:1084–93.
- [5] Bonilla JJ, Blanco JM, Lopez L, Sala JM. Technological recovery potential of waste heat in the industry of the Basque country. *Appl Therm Eng* 1997;17:283–8.
- [6] Desideri A, Gusev S, Van Den Broek M, Lemort V, Quoilin S. Experimental comparison of organic fluids for low temperature ORC (organic Rankine cycle) systems for waste heat recovery applications. *Energy* 2016;97:460–9.
- [7] Schuster A, Karella S, Kakaras E, Spliethoff H. Energetic and economic investigation of Organic Rankine Cycle applications. *Appl Therm Eng* 2009;29:1809–17.
- [8] Zhai H, Dai YJ, Wu JY, Wang RZ. Energy and exergy analyses on a novel hybrid solar heating, cooling and power generation system for remote areas. *Appl Energy* 2009;86:1395–404.
- [9] Fiaschi D, Lifshitz A, Manfrida G, Tempesti D. An innovative ORC power plant layout for heat and power generation from medium to low-temperature geothermal resources. *Energy Convers Manage* 2014;88:883–93.
- [10] Heberle F, Brüggemann D. Exergy based fluid selection for a geothermal Organic Rankine Cycle for combined heat and power generation. *Appl Therm Eng* 2006;30:1326–32.
- [11] Lentz A, Almanza R. Solar-geothermal hybrid system. *Appl Therm Eng* 2006;26:1537–44.
- [12] Dong LL, Liu H, Riffat SB. Development of small-scale and micro-scale biomass-fuelled CHP systems – a literature review. *Appl Therm Eng* 2009;29:2119–26.
- [13] Qiu G, Liu H, Riffat S. Expanders for micro-CHP systems with organic Rankine cycle. *Appl Therm Eng* 2011;31(16):3301–7.
- [14] Tchaneche BF, Lambrinos GR, Frangoudakis A, Papadakis G. Low-grade heat conversion into power using organic Rankine cycles – a review of various applications. *Renew Sust Energy Rev* 2011;5:3963–79.
- [15] Tempesti D, Manfrida G, Fiaschi D. Thermodynamic analysis of two micro CHP systems operating with geothermal and solar energy. *Appl Energy* 2012;97:609–17.
- [16] Talluri L, Lombardi G. Simulation and design tool for ORC axial turbine stage. *Energy Proc* 2017;129:277–84.
- [17] Fiaschi D, Manfrida G, Maraschillo F. Thermo-fluid dynamics preliminary design of turbo-expanders for ORC cycles. *Appl Energy* 2012;97:601–8.
- [18] Fiaschi D, Manfrida G, Maraschillo F. Design and performance prediction of radial ORC turboexpanders. *Appl Energy* 2014;138:517–32.
- [19] Fiaschi D, Innocenti G, Manfrida G, Maraschillo F. Design of micro radial turboexpanders for ORC power cycles: from 0D to 3D. *Appl Therm Eng* 2016;99:402–10.
- [20] Garg P, Karthik GM, Kumar P, Kumar P. Development of a generic tool to design scroll expanders for ORC applications. *Appl Therm Eng* 2016;109:878–88.
- [21] Lemort V, Quoilin S, Cuevas C, Lebrun J. Testing and modeling a scroll expander integrated into an Organic Rankine Cycle. *Appl Therm Eng* 2009;29(14–15):3094–12102.
- [22] Ziviani D, Van Den Broek M, De Paepe M. Geometry-based modeling of single-screw expander for organic rankine cycle systems in low-grade heat recovery. *Energy Proc* 2014;61:100–3.
- [23] Rice W. Tesla turbomachinery. Proceedings of the IV international Nikola Tesla symposium. 1991.
- [24] Tesla N. "Turbine", U.S. Patent No. 1061206; 1913.
- [25] Armstrong JH. An investigation of the performance of a modified Tesla turbine [MS. Thesis]. Georgia Institute of Technology; 1952.
- [26] Rice W. An analytical and experimental investigation of multiple-disk turbines. *J Eng Power* 1965;29:29–36. [ASME Press].
- [27] Carey VP. Assessment of Tesla Turbine Performance for Small Scale Rankine Combined Heat and Power Systems. *J. Eng. Gas Turbines Power* 2010;132:1–8.
- [28] Carey VP. Computational/theoretical modelling of flow physics and transport in disk rotor drag turbine expanders for green energy conversion technologies. In: Proceedings of the ASME 2010 international mechanical engineering congress & exposition. Vancouver (Canada); 2010.
- [29] Guha A, Sengupta S. The fluid dynamics of the rotating flow in a Tesla disc turbine. *Euro J Mech B/Fluids* 2013;37:112–23.
- [30] Sengupta S, Guha A. A theory of Tesla disc turbines. *Proc Inst Mech Engin, Part A: J Power Energy* 2012;226:651–63.
- [31] Guha A, Smiley B. Experiment and analysis for an improved design of the inlet and nozzle in Tesla disc turbines. *Proc IMechE, Part A: J Power Energy* 2009;224:261–77.
- [32] Hoya GP, Guha A. The design of a test rig and study of the performance and efficiency of a Tesla disc turbine. *Proc IMechE, Part A: J Power Energy* 2009;223:451–65.
- [33] Neckel AL, Godinho M. Influence of geometry on the efficiency of convergent-divergent nozzles applied to Tesla turbines. *Exp Therm Fluid Sci* 2014;62:131–40.
- [34] Lemma E, Deam RT, Tonich D, Collins R. Characterisation of a small viscous flow turbine. *Exp Therm Fluid Sci* 2008;33:96–105.
- [35] Schosser C, Fuchs T, Hain R, Lecheler S, Kahler C. Three-dimensional particle tracking velocimetry in a Tesla turbine rotor using a non-intrusive calibration method. In: 18th International symposium on the application of laser and imaging techniques to fluid mechanics. Lisbon; 2016.
- [36] Bloudíček P. Design of Tesla turbine. In: Theses conference. Brno (Czech Republic): Institute of Solid Mechanics, Mechatronics and Biomechanics; 2007.
- [37] Peshlakai A. Challenging the versatility of the tesla turbine: working fluid variations and turbine performance [MS. Thesis]. Arizona State University; 2012.
- [38] Krishnan V. Design and fabrication of cm-scale Tesla turbines [PhD Thesis]. California: Berkeley University; 2015.
- [39] Sengupta S, Guha A. Analytical and computational solutions for three-dimensional flow-field and relative pathlines for the rotating flow in a Tesla disc turbine. *Comput Fluids* 2013;88:344–53.
- [40] Guha A, Sengupta S. A non-dimensional study of the flow through co-rotating discs and performance optimization of a Tesla disc turbine. *J Power Energy Proc IMechE Part A* 2017;1–18.
- [41] Schosser C, Pfitzner M. A numerical study of the three-dimensional incompressible rotor airflow within a Tesla turbine. In: Conference on modelling fluid flow (CMFF'15); 2015.
- [42] Pandey RJ, Pudasaini S, Dhakal S, Uperty RB, Neopane HP. Design and computational analysis of 1 kW Tesla turbine. *Int J Scient Res Publ* 2014;4:11.
- [43] Choob TW, Rahman AA, Jer FS, Aik LE. Optimization of Tesla turbine using Computational Fluid Dynamics approach. In: IEEE symposium on industrial electronics and applications (ISIEA2011); 2011.
- [44] Lampart P, Kosowski K, Piwowarski M, Jedrzejewski L. Design analysis of Tesla micro-turbine operating on a low-boiling medium. *Pol Marit Res* 2009;28:33.
- [45] Lampart P, Jedrzejewski L. Investigations of aerodynamics of Tesla bladeless microturbines. *J Theoret Appl Mech* 2011;49(2):477–99.
- [46] Cirincione N. Design, construction and commissioning of an organic Rankine cycle waste heat recovery system with a Tesla hybrid turbine expander [MS. Thesis]. Colorado State University; 2011.
- [47] Bao G, Shi Y, Cai N. Numerical modelling research on the boundary layer turbine using organic working fluid. In: Proceeding of international conference on power engineering (ICOPE-13). Wuhan (China), 2013.
- [48] Song J, Gu CW, Li XS. Performance estimation of Tesla turbine applied in small scale Organic Rankine Cycle (ORC) system. *Appl Therm Eng* 2016;110:318–26.
- [49] Song J, Ren XD, Li XS, Gu CW, Zhang MM. One-dimensional model analysis and performance assessment of Tesla turbine. *Appl Therm Eng* 2018;134:546–54.
- [50] Manfrida G, Talluri L. Fluid dynamics assessment of the Tesla turbine rotor. In: Proceedings of ECOS 2016, June 19–23. Portoroz (Slovenia); 2016.
- [51] Manfrida G, Pacini L, Talluri L. A revised Tesla turbine concept for ORC applications. *Energy Proc* 2017;129:1055–62.
- [52] Lau SC, Sparrow EM, Ramsey JW. Effect of plenum length and diameter on turbulent heat transfer in a downstream tube and on plenum-related pressure losses. *J Heat Transfer* 1981;103:415–21.
- [53] Sparrow EM, Bosmans LD. Heat transfer and fluid flow experiments with a tube fed by a plenum having nonaligned inlet and exit. *Trans ASME, J Heat Transfer* 1983;105:56–62.
- [54] Harrison JA, Klemz BL. An investigation of the steady fluid flow within a simple plenum chamber. *High-Speed Surf Craft* 1982;32–4.
- [55] Anderson JD. Fundamentals of aerodynamics. 3rd ed. New York: McGraw Hill; 2001.
- [56] Shepherd DG. Principles of turbomachinery. New York: The Macmillan Company; 1956.
- [57] Shames IH. Mechanics of fluids. 4th ed. New York: McGraw-Hill Professional; 2002.
- [58] Butenko VA, Rylov YP, Chikov VP. Experimental investigation of the characteristics of small-sized nozzles. *Fluid Dyn* 1976;11:936–9.
- [59] Rohlik HE. Radial inflow turbines. NASA SP 290 1975;3:10.
- [60] Whitfield A, Baines NC. Design of radial turbomachines. Longman Scientific and Technical; 1990.
- [61] Klein SA, Nellis GF, "Mastering EES", f-Chart software, 2012.
- [62] Dixon SL. Fluid mechanics and thermodynamics of turbomachinery. 5th ed. Pergamon Press; 2005.
- [63] Ventura C, Jacobs P, Rowlands A, Petrie-Repar P, Sauret E. Preliminary design and performance estimation of radial inflow turbines: an automated approach. *J Fluids Eng* 2012. [ASME Press].
- [64] Munson RB, Okiishi TH, Huebsch WW, Rothmayer AP. Fundamentals of fluid mechanics. 7th ed. John Wiley and Sons, Inc.; 2013.
- [65] Idel'chik IE. Handbook of hydraulic resistance, coefficients of local resistance and of friction, 1st ed.; 1960.
- [66] McDonald AT, Fox RW. Effects of swirling inlet flow on pressure recovery in conical diffusers. *AIAA J* 1971;9(10).
- [67] Aljundi IH. Effect of dry hydrocarbons and critical point temperature on the efficiencies of organic Rankine cycle. *Renew Energy* 2011;36:1196–202.